

Chapter 7

Alloy Oxidation III: Multiphase Scales

7.1 INTRODUCTION

Practical heat-resisting alloys have multiple components (Tables 5.1 and 9.1), nearly all of which are susceptible to oxidation in a wide range of environments. When these alloys are exposed at high temperatures, an initial, transient period of reaction, in which all alloy components oxidise, is followed by a steady-state reaction. The rapid development of a corrosion resistant, steady-state scale morphology is the basis for alloy (or coating) design and selection and is the central concern of this chapter.

We wish to predict the nature of the steady-state reaction morphology as a function of alloy composition and environmental variables. Of particular interest are the conditions leading to the development of a protective, slow-growing oxide scale on the alloy surface. The ability of this scale to resist penetration by gaseous impurities such as sulphur and carbon is of obvious interest, as is also its ability to block outward diffusion of other alloy components. It turns out that diffusion through Cr_2O_3 scales of Fe, Ni and Mn is difficult to avoid, and simultaneous growth of two or more oxides has to be considered. As always, we wish to predict reaction rates and, ultimately, component lifetimes.

The prediction of steady-state reaction morphologies is a realistic goal for single oxidant environments, because the oxidant activity must decrease monotonically from the scale-gas interface to the alloy interior. The activity gradient provides the driving force for diffusion and interfacial mass transfer. Recognition of its existence permits the construction on phase diagrams of diffusion paths, if the alloy diffusion properties are known and concentration changes at the alloy-scale interface can be predicted.

Discussions of oxidation morphologies commenced with Wagner's analyses [1–4] of binary alloys. These distinguished alloy classes on the basis of the relative affinities for oxygen of the constituent metals. Subsequent reviews [5–7] have established a taxa of reaction morphologies for binary alloys based on the thermodynamic stabilities and transport properties of the oxidation products. Unfortunately, this systematic approach is not easily extended to

multicomponent alloys. Instead, we focus here on chromia and alumina scale formation and the processes which can accompany them. A brief review of binary alloy oxidation is followed by an examination of the effect of ternary alloy additions. Minority component effects are then considered, with particular attention directed to reactive element additions. Finally, the behaviour of alloys reacted with multiple oxidants is discussed. Consideration is restricted throughout to isothermal reaction conditions.

7.2 BINARY ALUMINA FORMERS

7.2.1 The Ni-Al System

Nickel-base alloys can be described using the phase diagram of Fig. 7.1. The γ -phase is the basis of the Inconel alloys, nickel-base superalloys have the $\gamma + \gamma'$ phase constitution and β -NiAl is a principal constituent of aluminide coatings, so this system is of considerable practical interest. The classic study of its oxidation behaviour was carried out by Pettit [8], using pure oxygen at 0.1 atm. His results are reproduced in the oxidation map of Fig. 7.2, which defines

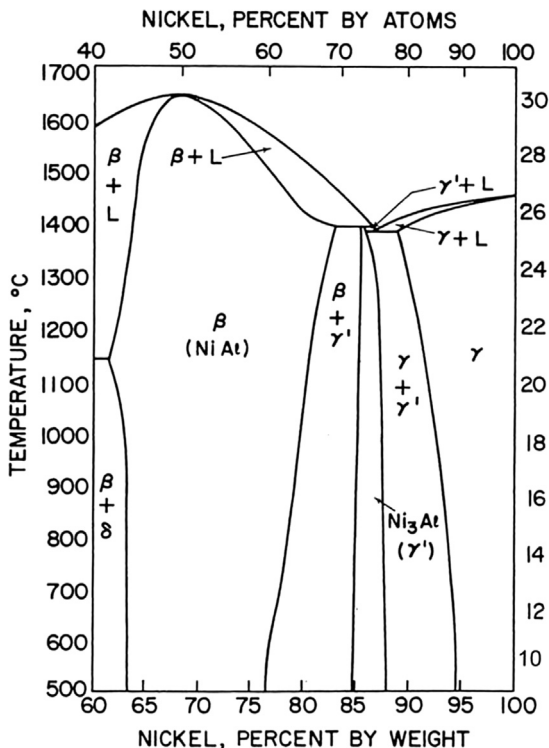


FIGURE 7.1 Ni-Al phase diagram.

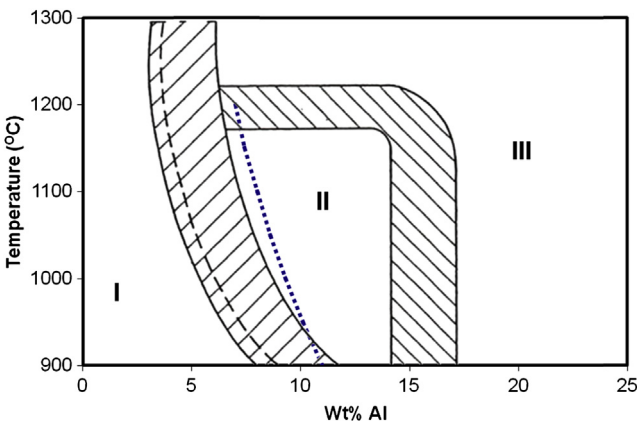


FIGURE 7.2 Oxidation map for Ni-Al alloys [8]. Reaction morphologies I, II and III are described in the text. Dotted line shows temperature dependence of $N_{Al,min}$ according to Eq. [7.6]. Dashed line shows $N_{Al,min}$ in CO/CO₂ (only Al₂O₃ stable).

regions I, II and III, corresponding to different reaction morphologies and mechanisms. The dilute alloys of region I developed external scales of NiO and internal precipitates of Al₂O₃ and NiAl₂O₄ at all temperatures investigated. In region II, a protective α -Al₂O₃ scale developed initially according to slow parabolic kinetics. Subsequently, however, a thick scale containing both NiO and spinel grew more rapidly, while a discontinuous alumina layer grew at and beneath the scale-alloy interface. Increasing either temperature or $N_{Al}^{(o)}$ changed the behaviour to type III, in which a protective α -Al₂O₃ scale was the only reaction product. The broad bands separating the regions arise through irregular behaviour, varying with alloy surface preparation.

Subsequent investigations have broadly confirmed these results. Hindam et al. [9–11] also found internal precipitation of Al₂O₃ and NiAl₂O₄ beneath a scale of NiO on dilute alloys, and irregular, nonreproducible kinetics for a Ni-6Al alloy followed by the development of a three-layered scale. The innermost layer was Al₂O₃, the intermediate layer NiAl₂O₄ and the outermost layer NiO. A scale of this type is shown in Fig. 7.3. Wood and Stott [12] identified the critical aluminium content necessary to form a stable Al₂O₃ scale at 1000°C as being in the range 7–12.5 wt%. More recently, Niu et al. [13] determined this critical level to be $N_{Al,min} = 0.10 - 0.15$ (5–7.5 wt%) at 1000°C. At the still lower temperature of 800°C, alloys containing up to 10 wt% Al undergo internal oxidation [14]. Thus there is disagreement as to the critical level at lower temperatures. The different reaction morphologies are readily understood in terms of diffusion paths mapped onto Ni-Al-O phases diagrams, such as that of Fig. 7.4. The dilute alloy situation is shown in Fig. 6.33. In essence, precipitation of Al₂O₃ and NiAl₂O₄ within the alloy depletes it so severely in aluminium that NiO is stable in contact with the metal. The situation for high

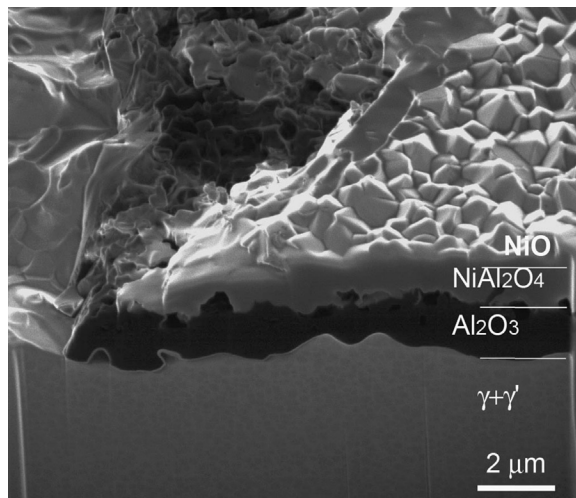


FIGURE 7.3 Three-layered scale grown on Ni-22Al shown in FIB milled section.

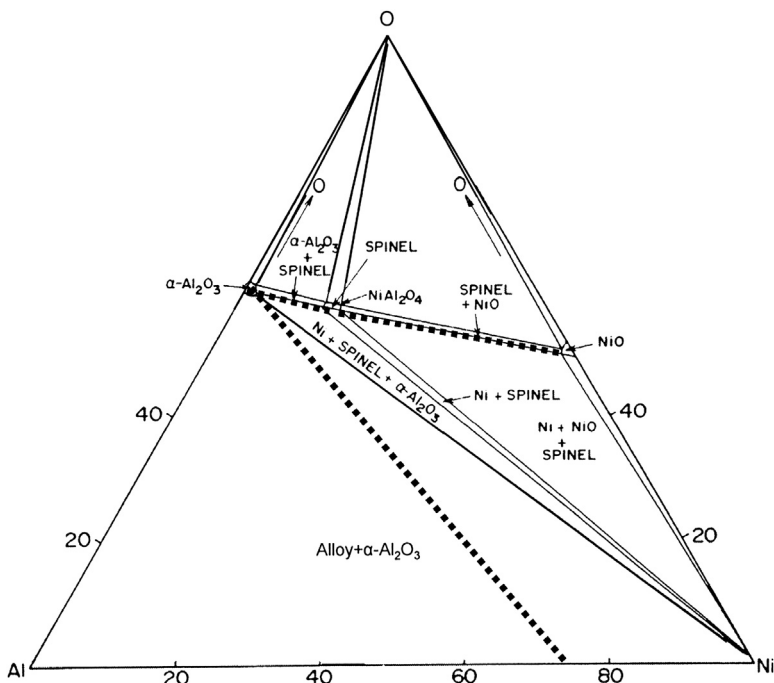
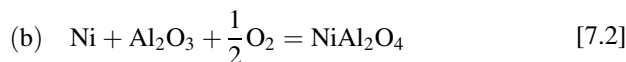


FIGURE 7.4 Ni-Al-O phase diagram section at 1000°C. Diffusion path for scale of Fig. 7.3 mapped as dotted line. Reproduced from F. Elrefaei, W.W. Smeltzer, *J. Electrochem. Soc.* 128 (1981) 2237, permission of The Electrochemical Society.

aluminium content alloys is shown in Fig. 5.24. If $N_{\text{Al}}^{(o)}$ is high enough, alumina forms in contact with the alloy, yielding Pettit's Type III reaction morphology. At lower N_{Al} (and higher N_{Ni}) values, the alumina scale is overlaid by spinel and NiO. This sequence reflects the relative stabilities of the oxides, as we now establish.

Reactions at the interface shown in the schematic diagram of Fig. 7.5 can be written as



on the basis that nickel diffuses through Al_2O_3 to form the outer layers. The oxygen activity at the scale-alloy interface clearly depends on a_{Al} . The minimum value of a_{Al} required to form Al_2O_3 , rather than nickel-rich oxides, can be estimated by the methods of Section 2.4. The requisite value of a_{Al} corresponds [8] to less than 1 ppm by weight, reflecting the very high stability of Al_2O_3 relative to NiO (Fig. 7.4). The actual value will depend on alloy diffusion. For high $N_{\text{Al}}^{(o)}$ values, depletion is minimal, and p_{O_2} values calculated from Eq. [7.1] are of order 10^{-30} atm at 1000°C. Turning next to reaction Eq. [7.2], the local equilibrium at interface (b) can be written

$$a_{\text{Ni}} p_{\text{O}_2}^{\frac{1}{2}} = \exp[\Delta G_f^\circ(\text{NiAl}_2\text{O}_4) - \Delta G_f^\circ(\text{Al}_2\text{O}_3)/RT] \quad [7.4]$$

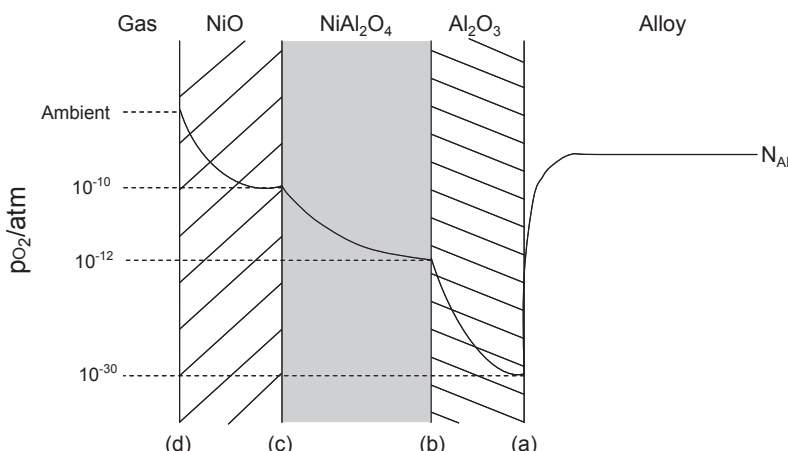


FIGURE 7.5 Schematic view of multiple scale grown on Ni-Al in Type II reaction. p_{O_2} values calculated for 1000°C, assuming $a_{\text{Ni}} = 1$.

where unit activity oxides have been assumed. Again the metal component activity will be controlled by diffusion. If it is low enough, as a result of the alumina layer blocking nickel diffusion, then spinel will not form at all. However, if nickel diffuses easily through the inner layer, its activity will be close to that of the alloy, ie, approximately unity. In this event, p_{O_2} is calculated from Eq. [7.4], using $\Delta G_f^\circ(NiAl_2O_4)$ from Table 7.1, to be of order 10^{-12} atm. For reaction at interface (c), a value of $p_{O_2} \approx 10^{-10}$ atm is calculated for $a_{Ni} \approx 1$ using $\Delta G_f^\circ(NiO)$ from Table 2.1. Thus the oxygen activity decreases monotonically from the outside to the inside of the scale, as it must for the scale to grow. Conversely, the oxide layers can be predicted to form in this sequence on the basis of their relative stabilities. The corresponding diffusion path is shown in Fig. 7.4.

Whilst the oxidation morphologies can be understood on the basis of Ni-Al-O thermodynamics, the conditions under which the regimes I, II and III develop cannot. These conditions are determined largely by kinetic factors, principally diffusion in the various phases. We consider first the boundary between internal and external oxidation, ie, between regions I and II.

Wagner's criterion [4] stated in Eq. [6.111] yields the minimum aluminium level, $N_{Al,min}$, necessary to form external scale rather than internal precipitate, if the critical precipitate volume fraction, g , for formation of a continuous layer is known. Nesbitt [16] set $g = 0.2$ and found, for 1200°C, that $N_{Al,min} = 0.07 - 0.09$ (4.4 wt%) at high p_{O_2} , where NiO can form. Using the more conventional value $g = 0.3$, and taking data for $D_o, N_o^{(s)}$ and D_{Al} from Chapter 2, the value $N_{Al,min} = 0.14$ at 1200°C, equivalent to 7 wt%, is calculated from these conditions. These two estimates lie within the transition band between internal and external alumina formation (Fig. 7.2). It is of interest to explore the effect of temperature on $N_{Al,min}$, with the aim of testing the utility of Wagner's expression in predicting the measured effect shown in Fig. 7.2.

TABLE 7.1 Spinel Free Energies of Formation

Spinel	$\Delta G_f^\circ = A + BT$ (J/mole)	
	A	B
FeCr ₂ O ₄	-1,450,670	324
NiCr ₂ O ₄	-1,376,880	332
MnCr ₂ O ₄	-1,583,600	331
FeAl ₂ O ₄	-1,988,442	406
NiAl ₂ O ₄	-1,933,667	408
MnAl ₂ O ₄	-2,119,897	414

Combining Wagner's condition (Eq. [6.111]) with Sievert's Eq. [2.71] for oxygen solubility, we obtain

$$N_{B,\min} = \left(g_{BO_v}^* \frac{\pi}{2v} \frac{V_A}{V_{BO_v}} \frac{K p_{O_2}^{1/2} D_o}{D_B} \right)^{1/2} \quad [7.5]$$

The temperature dependence of $N_{B,\min}$ can therefore be expressed as

$$R \frac{\partial \ln(N_{B,\min})}{\partial (1/T)} = \left(-\Delta \overline{H}_o - \Delta H(O_2) - Q_o + Q_B \right) / 2 \quad [7.6]$$

where $\Delta \overline{H}_o$ is the partial molar heat of dissolution of oxygen in solvent metal, $\Delta H(O_2)$ the enthalpy of the interface reaction producing $\frac{1}{2}O_2(g)$ and Q_i the activation energy for diffusion of the indicated species. The transition between regimes I and II is subject to the p_{O_2} value characteristic of the reverse of reaction Eq. [7.3], for which $\Delta H(O_2) = 234,200 \text{ J mol}^{-1}$. Taking $\Delta \overline{H}_o$ from Table 2.2 and the Q_i from Appendix D, the right-hand side of Eq. [7.6] is calculated as $21,828 \text{ J mol}^{-1}$. The predicted dependence of $N_{Al,\min}$ on temperature is shown as a dotted line in Fig. 7.2. Agreement with experiment is reasonably good for these high oxygen activity conditions.

Fig. 7.2 also shows results for the transition from internal to external alumina under low oxygen potentials, where only Al_2O_3 can form. These experiments were carried out in a CO/CO_2 gas mixture of fixed composition $p_{CO}/p_{CO_2} = 0.2$, so that p_{O_2} was controlled by the reaction $CO_2 = CO + \frac{1}{2}O_2$, for which $\Delta H(O_2) = 282,420 \text{ J}$. The enthalpy term in Eq. [7.6] is then evaluated as -4420 J , and the value of $N_{Al,\min}$ is predicted to increase with temperature. This is contrary to the experimental observations in Fig. 7.2. The calculated value of $N_{Al,\min}$ at $1200^\circ C$ is 0.05 (2.4 wt%), slightly less than the observed value of 3.0 wt%. It is possible that the slow gas-phase reaction led to a failure to achieve equilibrium, and the calculation for p_{O_2} is therefore inapplicable.

Despite the success of diffusion theory in accounting for the variation with temperature and $N_{Al}^{(o)}$ of the initial oxidation morphologies of Ni-Al alloys, it is evident from Fig. 7.2 that the formation of an initial alumina scale in region II did not correspond to long-term protection. Pettit [8] attributed this loss of protection to a lowering of the interfacial aluminium content, of $N_{Al,i}$, resulting from diffusion being slower than the rate of aluminium consumption by alumina scale growth. According to the Wagner description, if this was the case, no alumina scale could form in the first place. The two views are reconciled by recognising that behaviour in regime II is not steady-state, and Wagner's analysis therefore cannot apply. The nonsteady-state behaviour is explicit in the observed transition to approximately linear kinetics when protection is lost. This could result from a change in mass transfer mechanism within the scale, with any such change in the alloy being improbable.

Scale diffusion mechanisms can change in response to microstructural alterations or the precipitation of new phases. The slow diffusion of nickel into the alumina scale followed by formation of spinel and even NiO appears to be the reason for this behaviour. As pointed out by Pettit, it is prevented by increasing either $N_{\text{Al}}^{(o)}$ or the temperature, thereby maintaining a higher value of $N_{\text{Al},i}$ (and a lower $N_{\text{Ni},i}$). The effect of $N_{\text{Al}}^{(o)}$ is obvious, but the temperature effect implies that the activation energy for alloy diffusion (188 kJ/mol [17]) is greater than that of the alumina diffusion process.

Tracer diffusion studies have led to activation energy estimates of 477 kJ/mol for aluminium [18] and 460 kJ/mol for oxygen [19] in polycrystalline Al_2O_3 at high oxygen pressures and temperatures above 1450°C. However, extrapolation of these diffusion coefficients to the temperatures of oxidation experiments leads to values much lower than those implied by alumina scale growth rates. Hindam and Whittle [20] compared directly measured diffusion coefficient values with those deduced from alumina scaling rates. The results (Fig. 7.6) yielded approximate agreement for scale growth controlled by grain boundary diffusion of oxygen through a fine-grained (0.1–5 µm) structure (Eq. [3.113]).

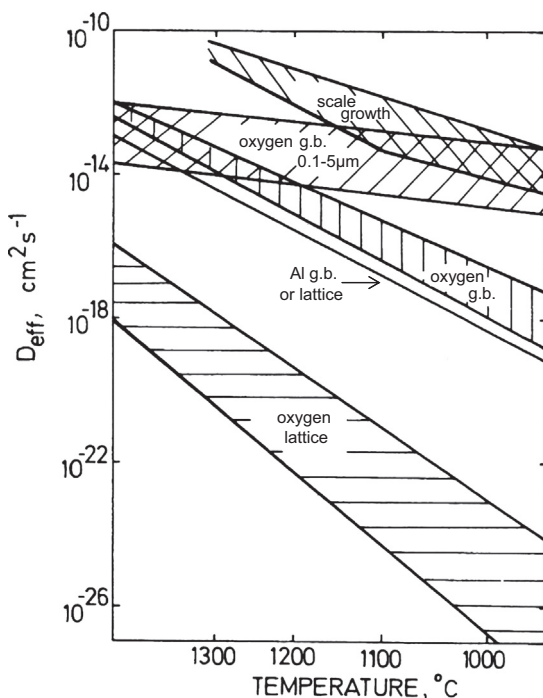


FIGURE 7.6 Comparison of diffusion coefficients deduced from alumina k_p values with diffusion data. With kind permission from H. Hindam, D.P. Whittle, *Oxid. Met.* 18 (1982) 245, Springer Science and Business Media.

The effective activation energy is 130 kJ/mol, less than that of alloy diffusion, as suggested by Petit.

Before leaving the Ni-Al system, it is appropriate to note that even when a protective scale is formed in regime III, the scale is not of practical use. The problem is that the scale cracks and spalls profusely on cooling from reaction temperature. Alloy developments aimed at preventing this problem are discussed in [Section 7.5](#).

7.2.2 The Fe-Al System

An isothermal section of the Fe-Al-O phase diagram is shown in [Fig. 7.7](#), and the Fe-Al diagram is shown in [Fig. 6.10](#). The Fe-Al-O diagram is similar to that of Ni-Al-O in that Al_2O_3 is by far the most stable oxide in both systems, with the consequence that all alloy compositions down to extremely low levels equilibrate with Al_2O_3 . Important differences exist with respect to oxide intersolubilities. The spinel and Fe_3O_4 form a continuous solid solution, and Al_2O_3 and Fe_2O_3 have limited mutual solubility, the extent of which increases at higher temperature. On the other hand, nickel has very little solubility in Al_2O_3 , and the NiAl_2O_4 spinel is a true ternary compound of closely stoichiometric composition.

Dilute Fe-Al alloys oxidise under Rhines pack conditions to produce internally precipitated aluminium-rich oxides [[23,24](#)]. Early work aimed at establishing aluminium levels necessary to reduce alloy scaling rates have been reviewed by Tomaszewicz and Wallwork [[25](#)]. Boggs [[26](#)] found that at $T < 570^\circ\text{C}$ and $p_{\text{O}_2} \approx 1 \text{ atm}$, and aluminium levels of about 2.4 wt% were sufficient to form an inner scale layer of FeAl_2O_4 spinel. This layer acted as a

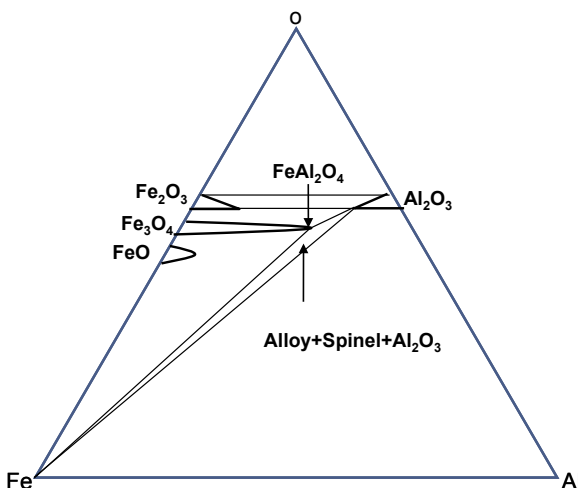


FIGURE 7.7 Phase diagram for Fe-Al-O. Data from L.M. Atlas, W.K. Susnida, *J. Am. Ceram. Soc.* 41 (1958) 150; J.A. Imlach, F.F. Glasser, *Trans. J. Br. Ceram. Soc.* 70 (1971) 227.

partial barrier to iron diffusion, reducing the thickness of the outer Fe_3O_4 layer by 75%. At higher temperatures, Al_2O_3 appeared in the scale in increasing amounts as the temperature increased to 800–900°C. The alumina was γ -phase at low temperatures, but increasingly α -phase at higher temperatures. At 800 and 900°C, an essentially pure Al_2O_3 film developed after the transient stage of reaction, and oxidation rates were very low. However, protection was lost after some time, and iron-rich nodules grew through the alumina, whilst aluminium was internally oxidised beneath the nodules. As seen in Fig. 7.8, a transparently thin Al_2O_3 layer covered most of the surface, but the sporadic nodules grew quickly, causing rapid attack on the alloys. This general pattern of reaction morphologies has been confirmed by others [27–31]. The minimum value of $N_{\text{Al}}^{(o)}$ necessary to prevent internal oxidation is 0.048 at 500°C [26] in the range 0.038–0.048 at 800°C [27] and 0.05 at 900°C [29]. The value required to form a protective alumina scale has been estimated as more than 0.15 at 600°C [26], 0.13 at 800°C [27] and 0.14 in the range 800–1000°C [32]. An investigation [33] into the oxidation of an Fe-Al alloy with $N_{\text{Al}}^{(o)} = 0.10$ at 1000°C confirmed that this was sufficient to prevent internal oxidation but not enough to stop nodule formation after an alumina scale was established.

The Fe-Al system is seen to be qualitatively similar to Ni-Al in possessing the same three regimes of behaviour. The same competition between oxygen diffusion into the alloy and aluminium diffusion to its surface determines the reaction morphology. Zhang et al. [33] have analysed the system at 1000°C in this way, making use of Wagner's criteria for scale formation. As noted in Section 6.3, depletion of aluminium from iron by either scale formation or

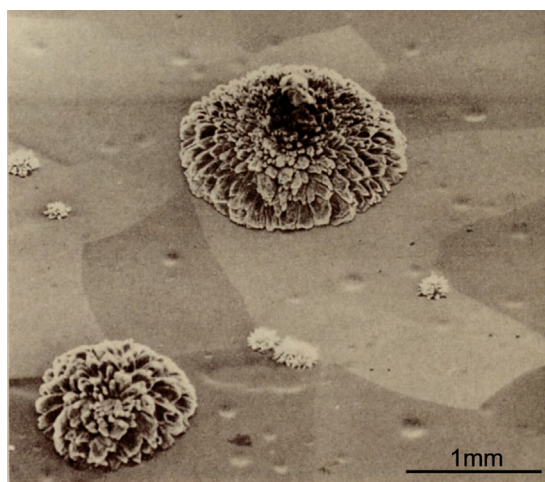


FIGURE 7.8 Iron-rich nodules growing out of thin alumina film on Fe-4.9 Al at 800°C, $p_{\text{O}_2} = 0.92$ atm. Reproduced from W.E. Boggs, J. Electrochem. Soc. 118 (1971) 906, permission of The Electrochemical Society.

internal precipitation causes the alloy $\alpha \rightarrow \gamma$ transformation. Unfortunately, data for D_{Al} in γ -Fe are unavailable. Using an estimate for this quantity, they calculated an $N_{\text{Al},\text{min}}$ of 0.04 to be required to prevent internal oxidation. Wagner's criterion for the N_{Al} value required to sustain a continuous Al_2O_3 scale (Eq. [5.22]) was found to yield 4.6×10^{-3} for α -Fe and 0.04 for γ -Fe. The experimental results for $N_{\text{Al}}^{(0)} = 0.10$ showed that internal oxidation did not occur, as predicted, but that iron-rich nodules or a mixed scale developed, and no continuous Al_2O_3 scale was maintained.

The same problem arises for Fe-Al as was noted for Ni-Al: Wagner's steady-state analyses do not succeed. The same reason is in effect: neither system achieves a long-lasting steady-state. In the case of Fe-Al, there is agreement that cracking of the alumina scale allows gas access to the underlying alloy. If this is depleted in aluminium, as might be the case if a subsurface γ -iron layer is present, then scale rehealing would be impossible, and iron-rich nodule formation thereby explained [26,27,31,34]. An alternative explanation suggested by Zhang et al. [33] is that iron oxides remaining from the initial period of transient oxidation react with the alumina, forming spinel. This decreases the Al_2O_3 layer thickness, balancing the growth process. If as a result the alumina layer thickness is approximately constant, aluminium metal is consumed according to linear kinetics, and depletion could be even more severe. Whether this could destabilise the alumina scale with respect to other oxides in the time scale required has not been established.

7.2.3 Transport Processes in Alumina Scales

Because $\alpha\text{-Al}_2\text{O}_3$ does not deviate measurably from stoichiometry, its native defect concentrations are extremely low and self-diffusion very slow. Despite the experimental difficulties, measurements of lattice diffusion have yielded a surprisingly self-consistent data set [35]. The important conclusions are that $D_{\text{O}} \ll D_{\text{Al}}$, and the activation energy for oxygen lattice diffusion is 585 kJ mol^{-1} . At 1100°C , $D_{\text{O}} \approx 10^{-15} \text{ cm}^2 \text{ s}^{-1}$, far too low to account for observed scaling rates. As noted earlier, grain boundary diffusion is much faster. In reviewing these data, Heuer et al. [36,37] set the grain boundary width $d = 1 \text{ nm}$, to estimate the boundary to lattice diffusion coefficient ratio $D_{\text{B}}/D_{\text{L}} \approx 10^5$ to 10^6 for oxygen at 1300 – 1500°C . Tracer diffusion data for grain boundary diffusion of aluminium are unavailable.

Agreement between different investigators on oxygen grain boundary diffusion coefficients is poor, with values differing by three or more orders of magnitude. Furthermore, the activation energies also differ, ranging from 627 to 884 kJ mol^{-1} , but are all greater than the value of 585 kJ mol^{-1} found for lattice diffusion. Before considering possible reasons for this result, recent results on oxygen permeability in polycrystalline alumina wafers are examined.

Schematic diagrams of the permeability experiment [38–40] and its results are shown in Fig. 7.9. Measurements were carried out at 1650 – 2000°C at both

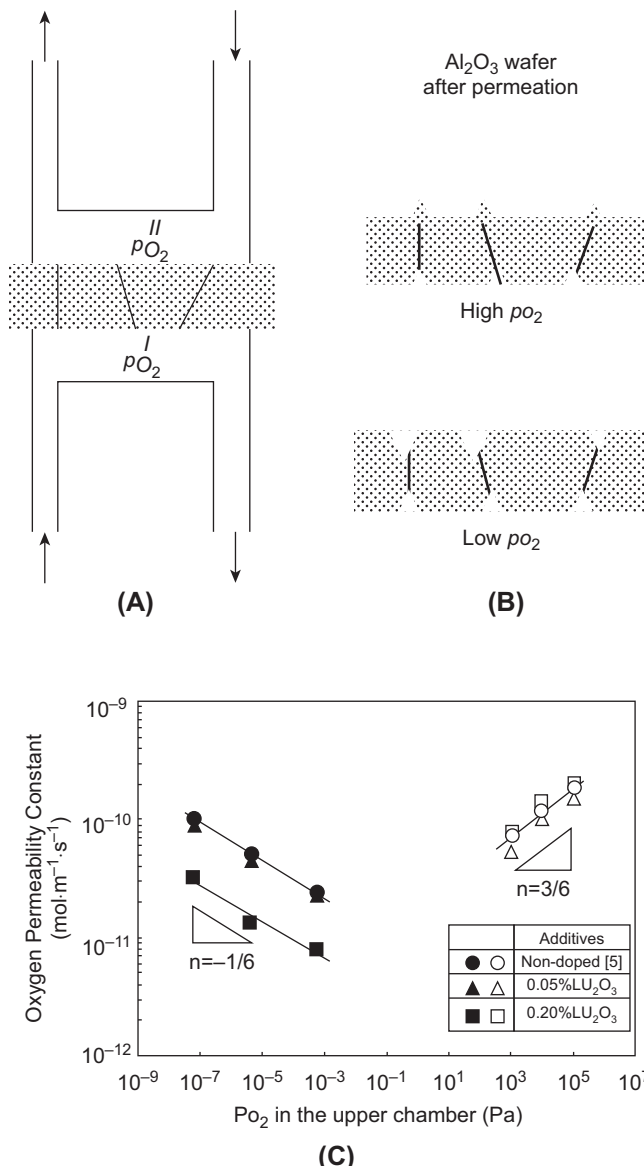
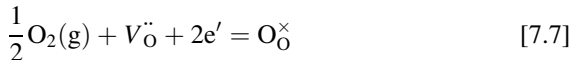


FIGURE 7.9 Alumina permeability (A) experimental arrangement ($p_{\text{O}_2}^{\text{II}} > p_{\text{O}_2}^{\text{I}}$); (B) cross-sections of alumina wafer after permeation; (C) grain boundary oxygen diffusion as a function of p_{O_2} . Part (C) reproduced from T. Matsudaira, M. Wada, T. Saitoh, S. Kitaoka, *Acta Mater.* 58 (2010) 1544, with permission from Elsevier.

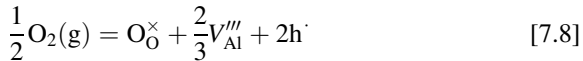
high and low oxygen pressures: 1 and 10^5 Pa or 10^{-8} and 1 Pa in the two chambers. The transfer of oxygen was measured by monitoring the oxygen levels in the inlet and outlet streams for each chamber. Oxygen was found to permeate the polycrystalline wafers in both the high and low oxygen pressure cases, but no permeation through a single crystal wafer was detected. Examination of the polycrystalline wafer surfaces revealed that the original mirror polish finish was modified by the high-temperature exposure. In the low oxygen pressure case, thermal grooving affected oxide grain boundaries on both sides of the wafer. In the high p_{O_2} experiment, grooving was again observed on the low pressure side, but oxide ridges had grown above the grain boundaries on the high pressure surface. These different effects were attributed to grain boundary diffusion of oxygen vacancies at low pressure, and aluminium vacancies at high pressure.

In the low p_{O_2} case, oxygen is absorbed at the higher pressure side of the wafer by occupying a vacant site



Vacancies diffuse through the wafer from the other side where they are generated by the reverse of Eq. [7.7], taking place at the lower oxygen partial pressure. Thus no net metal transfer occurs, the oxygen lost from one side of the membrane being replaced from the other.

In the high p_{O_2} case, there is a net metal transfer, with fresh alumina accumulating above grain boundaries on the higher pressure side. Clearly, metal diffuses counter current to the oxygen gradient in this case. It is proposed that metal vacancies form by uptake of oxygen at the high pressure side:



The vacancies then diffuse across the wafer, to be annihilated through the reverse of Eq. [7.8] at the lower oxygen pressure side, with the ejection of oxygen from the alumina. Thus it is suggested that alumina is p-type at high oxygen partial pressures and n-type at low oxygen pressures. The point defect models summarised here were supported by the observed p_{O_2} dependence of oxygen permeability.

Assuming that the only charged defects are oxygen vacancies and electrons at low oxygen pressure, and metal vacancies and positive holes at high p_{O_2} values, the charge balance may then be written as

$$[e'] = 2[V_O^{\cdot\cdot}] \quad \text{or} \quad [h^{\cdot}] = 3[V_{Al}^{\prime\prime\prime}] \quad [7.9]$$

Combination with Eq. [7.7] or Eq. [7.8] then leads to

$$[V_O^{\cdot\cdot}] = (4K_7)^{-1/3} p_{O_2}^{-1/6} \quad [7.10]$$

or

$$[V''']_{\text{Al}} = \left(\frac{K_8}{9}\right)^{3/8} p_{\text{O}_2}^{3/16} \quad [7.11]$$

As seen in Fig. 7.9, the observed permeability variation with p_{O_2} is in accord with Eq. [7.10] and Eq. [7.11], providing strong support for the defect model. It is also seen that the presence of lutetium slows grain boundary oxygen diffusion but has no effect on metal diffusion. Conversely, the presence of hafnium has been shown [41] to slow metal diffusion but has no effect on oxygen movement.

These impurity effects provide a possible explanation for the irreproducibility of grain boundary diffusion measurements made with notionally ‘pure’ polycrystalline alumina. The most energetically favoured native defects in alumina have been found from density function calculations [42] to be Schottky defects. However, the energy required for their formation is so large that native defect concentrations are extremely low. As shown in the permeability experiments, interaction with oxygen suffices to introduce higher defect concentrations, sufficient to support diffusion. The presence of impurities modifies oxygen permeation, presumably as a result of their segregation to grain boundaries, where defect motion is occurring. Different adventitious impurities in the alumina used by different investigators can therefore account for their widely varying results. The absence of this problem with oxygen lattice diffusion measurements is partially understandable: dilute impurities in single crystal alumina have no internal boundaries at which they can concentrate, only external surfaces. Within the crystal, they remain very dilute, and evidently exert little influence on lattice defects.

As recognised by Heuer et al. [36,37] and Smialek et al. [43], the oxygen permeability results provide the basis for prediction of scaling kinetics supported by grain boundary diffusion, provided that grain size is known. Because grain boundary diffusion is predominant, Eq. [3.133] is well approximated by

$$D_{\text{eff}} = f D_B \approx \frac{2dD_{\text{B,O}}}{D_{t,x}} \quad [7.12]$$

where the grain diameter, $D_{t,x}$, is in principle a function of both time and position within the scale. Substitution from Eq. [7.12] into the appropriate form of Eq. [3.62] then yields

$$k_p = \int_{a'_0}^{a''_0} \frac{2dD_{\text{B,O}}}{D_{t,x}} d \ln p_{\text{O}_2} \quad [7.13]$$

The oxygen grain boundary diffusion term found from the permeability measurements [40] is

$$dD_{\text{B,O}} = 1.52 \times 10^{-8} \exp\left(\frac{-467 \text{ kJ}}{RT}\right) p_{\text{O}_2}^{-1/6} \text{ cm}^3 \text{s}^{-1} \text{ atm}^{-1/6} \quad [7.14]$$

Combination of Eq. [7.13] and Eq. [7.14], followed by integration from one side of the scale to the other, leads to the result

$$k_{p,i} = -\frac{12A}{D_{t,x}} \left\{ (p''_{O_2})^{-1/6} - (p'_{O_2})^{-1/6} \right\} \approx \frac{12A}{D_{t,x}} (p'_{O_2})^{-1/6} \quad [7.15]$$

where $A = 1.52 \times 10^{-8} \exp(-467 \text{ kJ}/RT)$. Because p'_{O_2} is set by the alumina-alloy local equilibrium, its value is very low, leading to a faster rate of grain boundary diffusion than was observed at the pressures used in the permeability measurements.

The procedure leading to Eq. [7.15] is approximate, as it ignores the variation of $D_{t,x}$ with position within the scale. Furthermore, as the grain size changes with time, the kinetics cannot be parabolic. Nonetheless, the integration producing Eq. [7.15] is valid, because it is performed at a fixed time. For this reason, the rate constant evaluated here is termed the instantaneous parabolic rate constant, $k_{p,i} = X dX/dt$.

Measured parabolic rate constants [44–47] for several FeCrAl materials are compared in Fig. 7.10 with values calculated [43] from Eq. [7.15] using a grain size of 0.5 μm . Instantaneous values of k_p were calculated from original kinetic datasets at the reaction times when $D_{t,X} = 0.5 \mu\text{m}$ at the scale-alloy interface. These predicted values are seen in Fig. 7.10 to exceed experimental measurements by about an order of magnitude at 1200°C. The activation energy of the experimental rate data is 375 kJ mol⁻¹, whereas the value predicted from Eqs. [7.14] and [7.15] was 298 kJ mol⁻¹. The latter value differs from that of grain boundary diffusion because of the strong

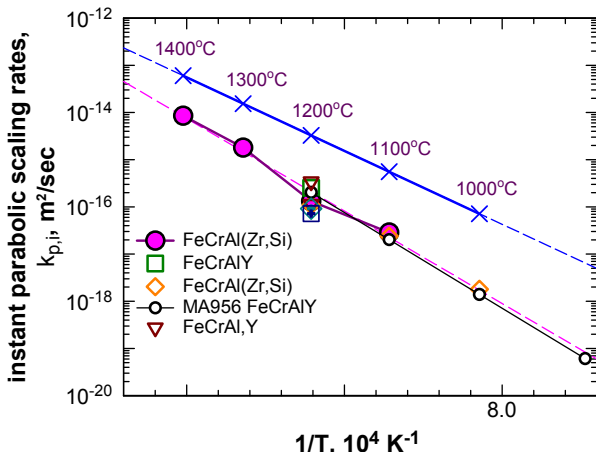


FIGURE 7.10 Ten experimental $k_{p,i}$ for alumina scale growth at grain size $D_{t,X} = 0.5 \mu\text{m}$ compared with prediction from permeability data: ● [43]; □ [44]; ◇ [45]; ○ [46]; ▽ [47]; -X-X- calculated [43] from Eq. [7.15]. Figure adapted from J.L. Smialek, N.S. Jacobson, B. Gleeson, D.B. Hovis, A.H. Heuer, NASA/TM – 2013-217855. with help of J. Smialek, NASA, Glenn.

temperature effect on p_{O_2} , controlled by the Al/Al₂O₃ equilibrium, Eq. [3.94]. The authors ascribed the overprediction of alumina scaling rates to the fact that the grain boundary permeability measurements derive from high purity alumina, whereas the rate data reflect the behaviour of impurity doped oxide.

An alternative approach is to treat the value of $D_{B,O}$ as a time and position-independent constant, representing an average value. This permits an investigation of the effect on scaling of a grain size which varies within the scale, as seen in Fig. 7.11. The relationship

$$D_{t,x} = a + bx \quad [7.16]$$

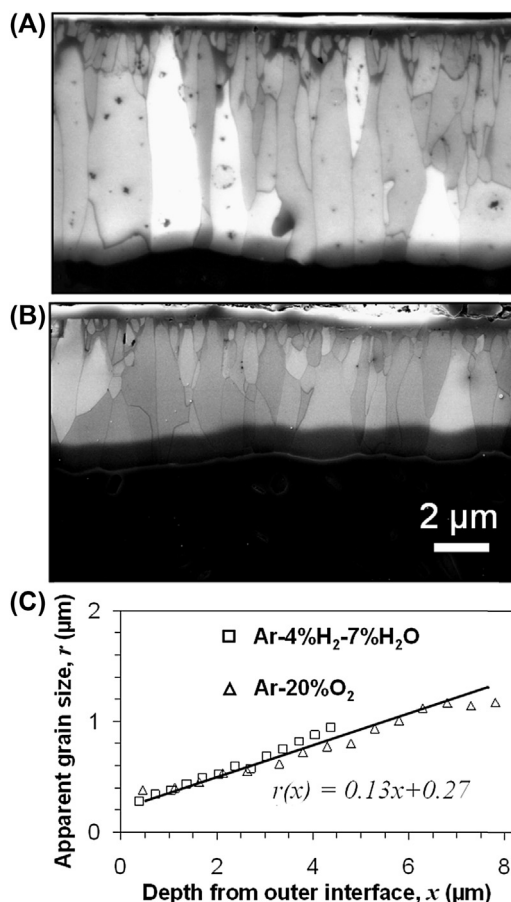


FIGURE 7.11 Microstructures of alumina scales grown on Fe-20Cr-5Al-0.05Y at 1250°C in O₂ and H₂/H₂O. With kind permission from D. Naumenko, B. Gleeson, E. Wessel, L. Singheiser, W.J. Quadakkers, Met. Mater. Trans. A 38A (2007) 2974, Springer Science and Business Media.

with x the position coordinate within the scale and a, b constants was found [48] to hold for scales grown on a model Fe-20Cr-5Al-0.05Y alloy in either O_2 or H_2/H_2O at temperatures of 1200–1300°C. In this case, Eq. [7.12] is rewritten as

$$D_{\text{eff}} = \frac{2dD_{\text{B},\text{O}}}{a + bx} \quad [7.17]$$

and the flux of oxygen is given by

$$J_{\text{O}} = -\frac{C}{RT} \frac{2dD_{\text{B},\text{O}}}{a + bx} \frac{\partial \mu_{\text{O}}}{\partial x} \quad [7.18]$$

with

$$\frac{dX}{dt} = J_{\text{O}} V_{\text{O}} \quad [7.19]$$

Here V_{O} is the molar volume of oxide formed by the diffusing species. As the kinetics are not parabolic, Eq. [7.18] is developed to yield J_{O} as a function of scale thickness.

In a nonporous scale of stoichiometric oxide, the flux is divergence free:

$$J_{\text{O}} \neq f(x) \text{ at } X, t \text{ constant} \quad [7.20]$$

and integration of Eq. [7.18] becomes possible. At a fixed value of X , rearrangement of Eq. [7.18] followed by integration yields

$$\mu_{\text{O}} = \mu''_{\text{O}} - \frac{J_{\text{O}} RT}{2CdD_{\text{B},\text{O}}} \left(ax + \frac{bx^2}{2} \right) \quad [7.21]$$

which is evaluated at the scale-alloy interface, $x = X$, to yield

$$J_{\text{O}} = \frac{4CdD_{\text{B},\text{O}}}{2aX + bX^2} \frac{\mu''_{\text{O}} - \mu'_{\text{O}}}{RT} \quad [7.22]$$

Combination of Eq. [7.19], Eq. [7.22] and the identity $CV_{\text{O}} = 1$ leads to the rate equation

$$\frac{aX^2}{2} + \frac{bX^3}{3} = \frac{4dD_{\text{B},\text{O}}\Delta\mu}{RT} t \quad [7.23]$$

This rate equation was found [48] to describe kinetic data for Fe-20Cr-5Al-0.05Y at 1200–1300°C very accurately. The corresponding average values of $dD_{\text{B},\text{O}}$ were 4×10^{-19} and $2 \times 10^{-18} \text{ cm}^3 \text{ s}^{-1}$ at 1200 and 1300°C, respectively. An activation energy for $dD_{\text{B},\text{O}}$ of 321 kJ mol⁻¹ was found. The apparently good agreement with the value of 298 kJ mol⁻¹ predicted from Eq. [7.14] is of limited reliability, as the temperature range for these measurements was small, only 100°C. Nonetheless, it seems that alumina scaling of FeCrAl alloys can be rather well-described using oxygen grain boundary permeability data combined with an accurate description of scale microstructures.

Finally, it is noted that an essential part of the calculation involves knowledge of p_{O_2} at the scale-alloy interface, and this can only be specified if a_{Al} in the alloy at this interface is known. In the case of ferritic alloys, aluminium depletion in the subsurface alloy is negligible, and the original alloy composition can be used, provided that the section thickness is reasonable. For austenitic alloys, however, diffusion is slower, and the interfacial value, $N_{Al,i}$, may need to be measured.

7.3 BINARY CHROMIA FORMERS

7.3.1 The Ni-Cr and Fe-Cr Systems

Isothermal sections of the Fe-Cr-O and Ni-Cr-O systems are shown in Figs. 2.5 and 5.7. The obvious difference between the two is the much greater intersolubility of oxides in the iron-based system. Thus a single phase field extends between the isotropic Fe_3O_4 and $FeCr_2O_4$ compositions, whereas the nickel spinel is a true ternary phase. This reflects the fact that a Fe^{3+} cation exists, but no such nickel species is formed. Similarly, a continuous Fe_2O_3 - Cr_2O_3 solid solution can form, whereas the nickel solubility in Cr_2O_3 is extremely small.

Oxidation morphologies for Fe-Cr and Ni-Cr, together with their associated diffusion paths, were discussed in Section 5.2. In both cases, the behaviour of dilute alloys is controlled by monoxide (MO) scale layer growth. Depending on temperature, internal precipitation of Cr_2O_3 is also observed. As the scale-metal interface advances, the Cr_2O_3 precipitates are incorporated into the scale and transformed into spinel. This reaction morphology is shown schematically in Fig. 7.12. The volume fraction of spinel increases with $N_{Cr}^{(o)}$ until the Cr_2O_3 phase appears. The extensive compositional range of the Fe-Cr spinel allows the formation of an almost continuous spinel layer on low chromium alloys, as illustrated by the 9Cr steel in Fig. 7.13.

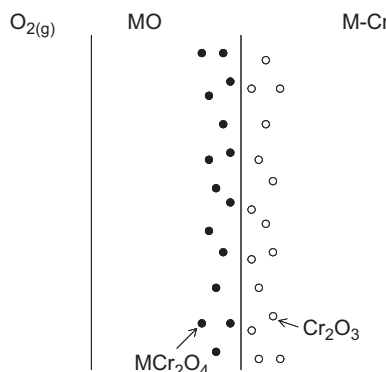


FIGURE 7.12 Schematic view of M-Cr alloy oxidation at subcritical $N_{Cr}^{(o)}$ levels. If M = Fe, outer layers of Fe_3O_4 and Fe_2O_3 form at high p_{O_2} values.

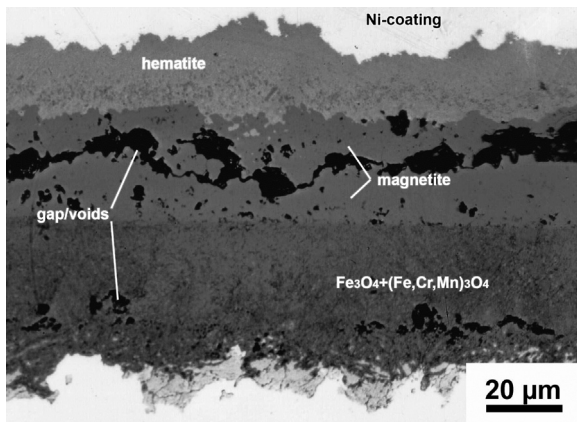


FIGURE 7.13 Spinel formation in inner scale layer grown on P91 steel at 650°C. Reprinted with permission from J. Ehlers, D.J. Young, E.J. Smaardyk, A.K. Tyagi, J. Penkalla, L. Singheiser, W.J. Quadakkers, *Corros. Sci.* 48 (2006) 3428, Elsevier.

These changes in morphology are reflected in oxidation rates. A compilation by Wood et al. [50] of oxidation rate data for model alloys is reproduced in Fig. 7.14. Very small additions of chromium increase the rate of nickel oxidation, but not that of iron. This is generally thought to be a dopant effect, due to an increase in V_M'' concentration to compensate for dissolved Cr_M^\bullet . It is not observed for Fe-Cr alloys, because $\text{Fe}_{1-\sigma}\text{O}$ is already highly defective. The decrease in rate observed as $N_{\text{Cr}}^{(o)}$ is further increased is due to a growing volume fraction of spinel particles within the MO layer. Because diffusion in the spinel phase is relatively slow, the particles effectively reduce the diffusional cross-section of the MO layer, slowing its growth. In addition, porosity develops within the MO+ spinel scale layer, because the two-phase oxide is unable to deform plastically to accommodate the volume loss caused by outward diffusion of iron or nickel. Gas-phase transport of oxygen within the pores is slow (Section 2.9) if O_2 is the only gas species available, and pore formation also slows scale growth.

The reduction in rate as alloy chromium levels are increased to about 10 wt% is much greater for Fe-Cr than for Ni-Cr. This difference is partly due to the fact that diffusion in NiO and NiFe_2O_4 is much slower than in iron oxides, and the basis for comparison therefore differs. It also reflects the more ready formation of a continuous spinel layer on Fe-Cr alloys. The limited intersolubility of NiO and NiCr_2O_4 means that the latter phase remains as dispersed particles, providing much less diffusional blocking.

At higher chromium levels, continuous scales of Cr_2O_3 develop, and the rate constant drops sharply (Fig. 7.14). The chromium levels predicted from Eq. [7.5] to be necessary for chromia scale formation are shown in Table 6.8. They are in only approximate agreement with the experimental results of

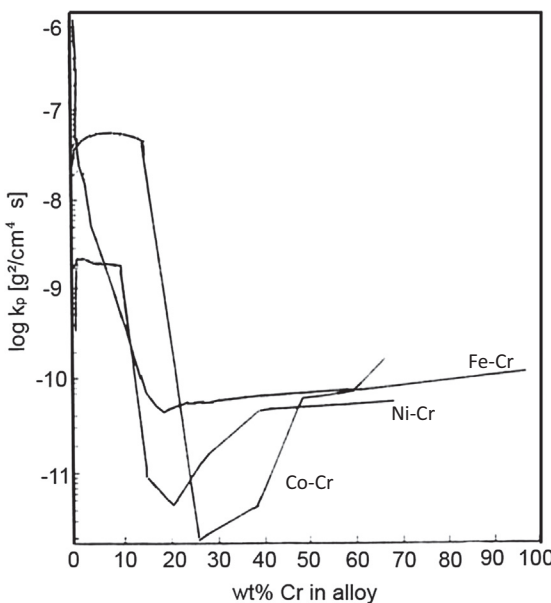


FIGURE 7.14 Oxidation rates of M-Cr alloys in pure O_2 at 1000°C. Reproduced with permission G.C. Wood, I.G. Wright, T. Hodgkiss, D.P. Whittle, Werkst. Korros 21 (1970) 900, from Wiley-VCH.

Fig. 7.14. The slower rate of chromia scaling on nickel-base alloys is attributed to more severe chromium depletion resulting from its slower diffusion in these alloys. Under these circumstances, alloy diffusion contributes to oxidation rate control [51], as discussed in Section 5.4.

Iron-base alloys with chromium levels near the critical value $N_{\text{Cr},\min}$ do not achieve long-term oxidation resistance. The high solubility in Cr_2O_3 of iron permits its outward diffusion and the formation of iron-rich oxides at the scale surface. Chromium levels of about 25 wt% are required to prevent this. Nickel-base alloys are superior in this respect, partly as a consequence of the much lower solubility of nickel in Cr_2O_3 , and perhaps reflecting also differences in diffusion coefficients, as is discussed below.

In order to understand more fully the difference between Fe-Cr and Ni-Cr oxidation and to analyse the effects of additional alloy components, it is necessary to consider diffusion in the scale.

7.3.2 Transport Processes in Chromia Scales

Much of the early data on Cr_2O_3 scale growth rates and mechanisms have been reviewed by Kofstad [53], who concluded that chromia scales grow by outward diffusion of chromium. Although the defect properties of Cr_2O_3 are not fully understood (see Section 3.9.2), subsequent work has shown that grain

TABLE 7.2 Values of Lattice Diffusion Coefficient, D_L , Grain Boundary Diffusion Coefficient, D_B times Boundary Width, d , and Grain Size, D_t in Cr_2O_3 Scales at 900°C [58]

Base alloy	Diffusant	$D_L/(\text{cm}^2 \text{s}^{-1})$	$dD_B (\text{cm}^3 \text{s}^{-1})$	$D_t (\mu\text{m})$
Fe-20Cr	Fe	2×10^{-14}	1×10^{-16}	0.1
	Ni	3×10^{-15}	2×10^{-19}	0.2
	Mn	2×10^{-14}	2×10^{-17}	0.1
	Cr	1×10^{-14}	1×10^{-16}	0.1
Fe-20Cr-12Ni	Fe	4×10^{-15}	1×10^{-17}	0.1
	Ni	5×10^{-15}	5×10^{-19}	0.2
	Mn	2×10^{-13}	—	0.4
	Cr	7×10^{-15}	2×10^{-17}	0.1

boundary diffusion is much faster than lattice diffusion for both chromium [54,55] and oxygen [55–57]. These data indicate that chromia growth on simple binary alloys is supported mainly by chromium diffusion, but oxygen diffusion also contributes to overall mass transport.

For spinel MCr_2O_4 to grow on top of the Cr_2O_3 scale layer, the metal M must also diffuse outwards. Lobnig et al. [58] studied the diffusion of vacuum deposited Fe, Ni, Mn and Cr into thin (1–2 μm) Cr_2O_3 scales which had been grown on Fe-20Cr or Fe-20Cr-10Ni alloys. By analysing the penetration profile shapes, they determined the diffusion coefficient values shown in Table 7.2 for short diffusion times. Assuming a value for the boundary width $d = 1 \text{ nm}$, the D_B values for Fe, Cr and Ni were found to be several orders of magnitude greater than the corresponding lattice diffusion coefficients. Surface roughness led to inaccuracies in the estimates of both D_L and D_B , but the errors were small compared with the orders of magnitude differences in the data of Table 7.2.

Using Eq. [3.113] to calculate effective values, D_{eff} , and for simplicity, assuming cubic oxide grains, we see that $D_{\text{eff}}(\text{Cr})$ has closely similar values in the two scales: 10^{-15} to $10^{-14} \text{ cm}^2 \text{s}^{-1}$. Furthermore $D_{\text{eff}}(\text{Fe}) \approx D_{\text{eff}}(\text{Cr})$ for Fe-20Cr, thereby explaining the rapid growth of an outer FeCr_2O_4 layer on high iron activity alloys. The values of $D_{\text{eff}}(\text{Ni})$ are, in the Fe-20Cr scale, an order of magnitude lower than that of chromium, but in the Fe-20Cr-12Ni scale, about half that of chromium. In the absence of a value for a Ni-Cr scale, the data for $D(\text{Ni})$ seem inconclusive.

The relatively large value of $D_{\text{eff}}(\text{Fe})$ in Cr_2O_3 is relevant to the technique of ‘preoxidation’. This is the method of first oxidising an alloy at low p_{O_2} so

that FeO is unstable and the selective oxidation of chromium assured. After a protective Cr₂O₃ scale has formed, the alloy is placed into service at what will usually be a higher p_{O_2} value. Unfortunately, the high oxygen pressure provides a gradient in a_O which constitutes a driving force for iron diffusion through the chromia scale to form iron oxide. Preoxidation of Fe-9Cr and Fe-7.5Cr in H₂/H₂O ($p_{O_2} = 6 \times 10^{-20}$ atm) at 850°C produced chromia scales of about 1 μm thickness [59]. Subsequent exposure, without change in temperature, to pure oxygen at 1 atm led to continued slow growth of these scales until the rates accelerated with the precipitation of iron-rich oxide at the scale-gas interface after 2–3 weeks. Taking $D_{\text{eff}}(\text{Fe}) = 1 \times 10^{-15}$ cm² s⁻¹ and estimating the iron diffusion penetration distance as

$$X^2 \approx 4D_{\text{eff}}(\text{Fe})t \quad [7.24]$$

a penetration time of 29 days is calculated for a 1 μm scale. Agreement with the experimentally observed times for iron to reach the chromia scale surface can be regarded as satisfactory, given the approximate basis of Eq. [7.24] and the uncertainty in the value of $D_{\text{eff}}(\text{Fe})$. It is concluded that preoxidation of marginal Fe-Cr alloys needs careful investigation before use. The high-temperature growth of relatively thick Cr₂O₃ scales before service at substantially lower temperatures could nonetheless prove successful.

7.4 TERNARY ALLOY OXIDATION

Our interest is in alloys for which selective oxidation of one component leads to the development of a slow growing, protective scale. We therefore consider firstly alloys in which one component is much more reactive to oxygen than the other two, and secondly alloys in which two components are each much more reactive than the third. The first case is exemplified by Fe-Ni-Cr, the basis of heat-resisting steels, and Ni-Pt-Al, the basis of a number of high-temperature coatings. Examples of the second are Fe-Cr-Al (Kanthal) and Ni-Cr-Al (superalloys and Inconels). In many cases the reactive metals can be regarded as solutes in iron and/or nickel, although they may also partition to minority phases.

7.4.1 Fe-Ni-Cr Alloys

Single-phase Fe-Ni-Cr alloys should in principle be easily understood. However, accurate prediction of $N_{\text{Cr},\text{min}}$ even for binary alloys was found to be difficult (Table 6.8). At this time it cannot even be attempted for the ternary alloys, because data for $N_o^{(s)}$ and D_o in Fe-Ni binaries are not available. In the case of attack by carbon, the necessary data are available and provide a quantitative description of Fe-Ni-Cr carburisation (Chapter 9). In the absence of such data for oxidation, a discussion is necessarily qualitative. As seen in Fig. 7.15, differences between the Fe-Cr and Ni-Cr systems are reflected in

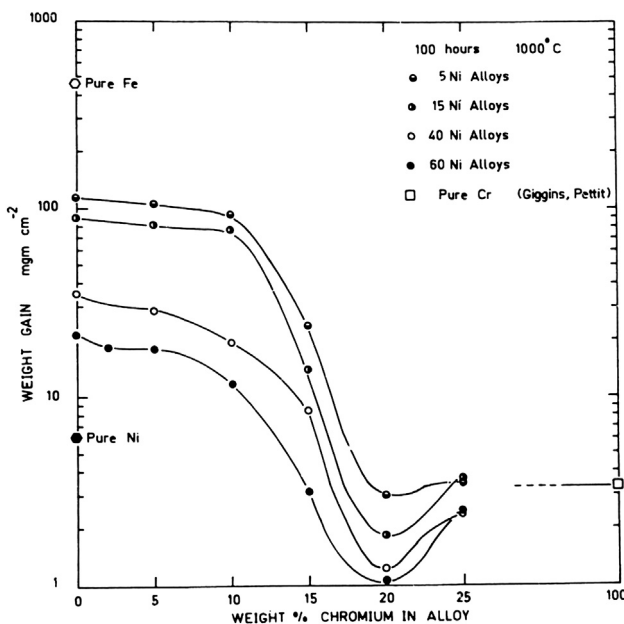


FIGURE 7.15 Oxidation weight gains of Fe-Ni-Cr alloys reacted in pure O_2 at $1000^\circ C$ for 100 h. With kind permission from J.E. Croll, G.R. Wallwork, *Oxid. Met.* 4 (1972) 121, Springer Science and Business Media.

ternary alloy oxidation rates. For a given chromium level, oxidation rates decrease with an increase in the Ni/Cr ratio. At chromium levels less than about 10%, the differences reflect changing volume fractions of $Fe_{1-\delta}O$ and the slower diffusing $Ni_xFe_{3-x}O_4$, and at high nickel levels, $NiFe_2O_4$ and NiO [52].

Scales formed on alloys with more than about 20% chromium consisted of an inner Cr_2O_3 layer, overlaid by spinel. Increases in Ni/Fe ratio led to decreases in alloy iron activity and its consequently smaller solubility in Cr_2O_3 . This in turn affected the extent of spinel formation. The behaviour shown in Fig. 7.15 is relevant to the performance of heat-resisting steels, which typically contain about 10–20 wt% nickel and are austenitic. At the higher N_{Ni} levels, long-term protection against iron spinel formation can be achieved. Consequently, austenitic stainless and heat-resisting steels based on formulations in the range Fe-(10–20) Ni-(20–25) Cr are widely used at temperatures up to 900–1100°C, depending on the atmosphere.

7.4.2 Ni-Pt-Al Alloys

It has been known for some time [60–62] that the addition of platinum to nickel aluminide intermetallics improves their oxidation resistance. Platinum-modified

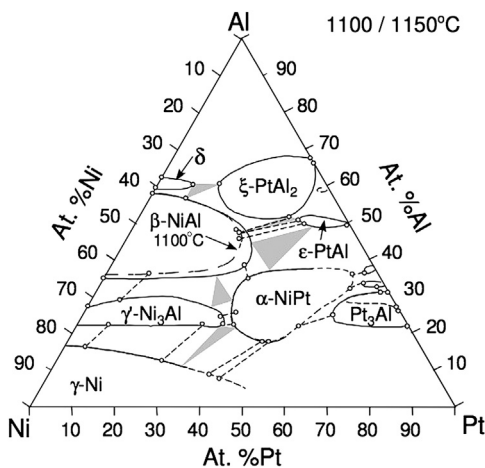
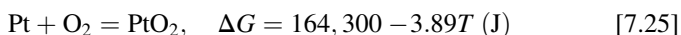


FIGURE 7.16 Isothermal section ($T = 1150^\circ\text{C}$) of Ni-Pt-Al phase diagram. Reprinted from S. Hayashi, S.I. Ford, D.J. Young, D.J. Sordelet, M.F. Besser, B. Gleeson, *Acta Mater.* 53 (2005) 3319, with permission from Elsevier.

β -NiAl is used as a bondcoat on superalloy components in turbines [63] (Section 1.3), and new coatings based on γ/γ' constitutions have been investigated [64–66]. An isothermal section of the Ni-Pt-Al phase diagram in Fig. 7.16 shows that the solubility of platinum in each of the γ , γ' and β -phases is large. Copland [68,69] has shown that substitution of platinum for nickel in these phases at constant N_{Al} has the effect of reducing the a_{Al} value.

Platinum is not completely inert to oxygen at high temperatures, instead forming a volatile oxide.



If $p_{\text{O}_2} = 1 \text{ atm}$, then p_{PtO_2} values of 2×10^{-6} to $4 \times 10^{-5} \text{ atm}$ are predicted for 1100 – 1200°C . However, exposure of platinum-bearing nickel aluminides to oxygen or air leads to the growth of external scales which protect the platinum from oxidation.

Oxidation of β -NiAl produces a scale of pure Al_2O_3 . Although this behaviour is in regime III of Pettit's classification (Fig. 7.2), the reaction rate is determined by which alumina phase grows (Section 5.7) and the frequency of scale spallation. The extent of spallation, which can occur under isothermal conditions, is determined by cavity formation at the scale-alloy interface (Section 5.8) and the amount of impurity sulphur in the system [70–75]. The nature of the sulphur effect is discussed in Section 7.5. For present purposes, the important finding is that the addition of platinum to β -NiAl suppresses spallation.

The cavities developed at a β -NiAl/ Al_2O_3 interface (Fig. 5.12) are observed even in the very early stages of reaction [76,77]. The addition of platinum to the intermetallics decreases both their size and number density,

whether or not sulphur is present in the alloy [78–81]. This decrease in void volume fraction is not due to any decrease in the amount of aluminium oxidation. In fact, alumina scaling rates are accelerated by the presence of platinum [82,83], as shown in Fig. 7.17. As is discussed in Section 5.8, the cavities are Kirkendall voids, and their accumulation represents the mismatch between aluminium and nickel alloy fluxes. These fluxes are driven

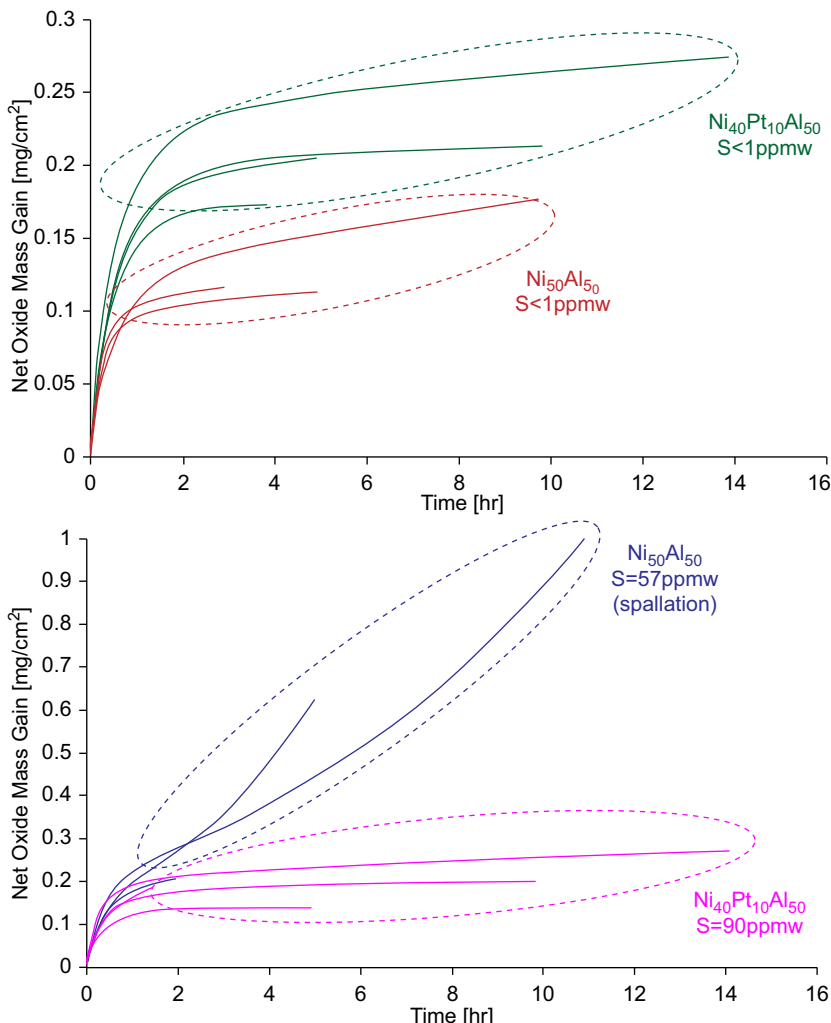


FIGURE 7.17 Effect of Pt on NiAl oxidation at 1100°C for low and high sulphur alloys. With kind permission from Y. Cadoret, D. Monceau, M.-P. Bacos, P. Jossos, V. Maurice, P. Marcus, *Oxid. Met.* 64 (2005) 185, Springer Science and Business Media.

by the chemical potential gradients arising from the concentration profiles in the alloy (Fig. 5.48):

$$J_i = -C_i B_i \frac{\partial \ln a_i}{\partial x} \quad [7.26]$$

The presence of platinum depresses a_{Al} , increasing the chemical potential gradient and hence the flux of aluminium. This accounts for the reduction of Kirkendall porosity. It also supports the more rapid alumina scale growth observed for β -Ni(Pt)Al. The increased D_{Al} in Ni(Pt)Al has been observed directly in diffusion couple studies [65]. The decrease in cavity formation decreases the amount of bare metal surface beneath the oxide where sulphur may segregate.

Somewhat similar effects are observed for γ' and γ/γ' alloys when platinum is added. In the absence of platinum, these alloys fall in regime II of Fig. 7.2 and are marginal alumina formers, growing NiO and $NiAl_2O_4$ on top of their alumina scales. When platinum is added to the alloys, NiO formation is decreased and suppressed completely at high platinum levels [84]. Gleeson et al. [65,84] ascribe this to two effects: the chemical potential gradient effect described above, and the decrease in oxygen permeability in the γ -phase observed with increasing platinum levels. As seen in Eq. [7.5], such a decrease reduces the initial value of $N_{Al}^{(o)}$ required to form external rather than internal Al_2O_3 .

The addition of platinum to Ni-Al alloys can profoundly affect their oxidation behaviour, despite the fact that platinum does not participate directly in the oxidation process. The effects arise out of the strong interactions within the alloy between platinum and the other constituents. These change a_{Al} values, and hence aluminium diffusion rates, and appear also to lower oxygen permeabilities, at least in the γ -phase. Faster aluminium diffusion not only helps stabilise the alumina scale, but decreases the amount of Kirkendall voidage.

Attention is now directed to the technologically important M-Cr-Al alloys, where M is Fe or Ni. Whilst also important, Co-Cr-Al alloys are less commonly used and will not be discussed here. It is important to enquire into the circumstances under which these alloys act as chromia or alumina formers. A very large and complex literature has accumulated in this area, extensive reviews of which have been provided by Wood and Stott [85] and Stott et al. [86].

7.4.3 Ni-Cr-Al Alloys

The phase constitutions of these alloys [87] can be seen in Fig. 5.36. The γ -Ni phase has extensive solubilities for both aluminium and chromium, and the Ni-Al intermetallics have smaller, but significant solubilities for chromium. The construction of a three-dimensional quaternary Ni-Cr-Al-O diagram is

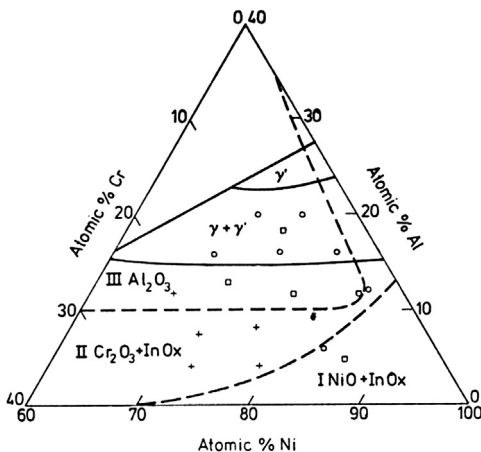


FIGURE 7.18 Oxide map for Ni-Cr-Al ternaries at 1000°C. With kind permission from G.R. Wallwork, A.Z. Hed, *Oxid. Met.* 3 (1971) 171, Springer Science and Business Media.

unrewarding. Instead, a concise way of describing the oxidation behaviour of such a broad range of alloy compositions and correspondingly diverse set of phase assemblages is provided by oxide mapping [88–91]. Compositional regions in which particular oxides predominate in the steady-state scale are plotted onto the Gibbs triangle. The map proposed by Wallwork and Hed [89] for Ni-Cr-Al at 1000°C is shown in Fig. 7.18. Although empirical, these maps can be very useful, for example in indicating the relationship between the Ni/Cr ratio and the ability to form a highly protective alumina scale.

The thermodynamics of the oxide system are useful in understanding the development of different reaction morphologies. We enquire as to where chromium-rich oxides would be stable in the oxide layer sequence, shown in Fig. 7.5, by altering the alloy to Ni-Cr-Al and considering the reaction



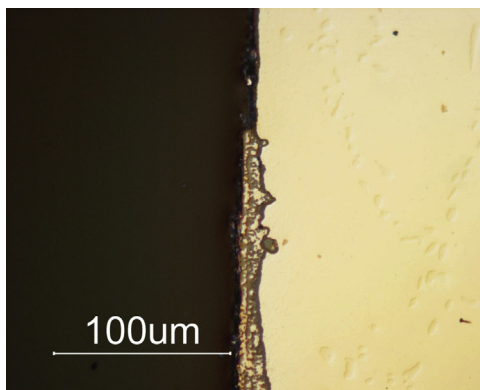
for which the equilibrium condition is

$$a_{\text{Cr}}/a_{\text{Al}} = \exp\{-[\Delta G_f^\circ(\text{Al}_2\text{O}_3) - \Delta G_f^\circ(\text{Cr}_2\text{O}_3)]/2RT\} \quad [7.28]$$

Alumina is much more stable than chromia (Table 2.1), and a value of $a_{\text{Cr}}/a_{\text{Al}} = 3.6 \times 10^8$ is calculated for 1000°C. It is therefore concluded that Cr_2O_3 could be stable in contact with an alloy only if $N_{\text{Al}}/N_{\text{Cr}} \leq 3 \times 10^{-9}$. Put another way, the equilibrium oxygen potential at a Cr_2O_3 -alloy interface is much higher than the value required to oxidise aluminium at any significant concentration. Thus it is concluded that alumina will form beneath a chromia layer, either as a continuous layer or as an internal precipitate. Examples are shown in Figs. 5.1(c) and 7.19.

The development of these morphologies was clarified by the transient oxidation studies carried out by Pettit et al. [91,92] on alloys containing

FIGURE 7.19 Alumina layer (black) developing on Ni-9Fe–26Cr-2.7Al.



2–30Cr and 1–9Al at 1000–1200°C. Rapid initial reaction formed a scale principally of mixed spinel, $\text{Ni}(\text{Cr},\text{Al})_2\text{O}_4$ plus isolated grains of NiO and Cr_2O_3 . The a_{o} value corresponding to the spinel–alloy equilibrium is higher than the values required to form either Cr_2O_3 or Al_2O_3 . The more abundant chromium consequently reacted with spinel to form a continuous Cr_2O_3 . Reaction Eq. [7.27] then took place at the scale-alloy interface producing transient alumina phases. These subsequently transformed into $\alpha\text{-Al}_2\text{O}_3$ which coalesced to form a continuous, but nonuniform layer. The remnants of NiO and Cr_2O_3 on the outside of the alumina layer were then isolated from the alloys and ceased to grow. At these high temperatures, the chromia was eventually lost as vapour through reaction Eq. [1.35], and the NiO was incorporated into the scale.

It is important to note that $\alpha\text{-Al}_2\text{O}_3$ is more easily formed and maintained as an external scale on Ni-Cr-Al alloys than on Ni-Al alloys. This is explicit in the oxide maps of Figs. 7.2 and 7.18. We will return to this point after first reviewing briefly the Fe-Cr-Al system.

7.4.4 Fe-Cr-Al Alloys

The Fe-Cr-Al system provides the basics for Kanthal and similar alloys (Table 5.1). The interesting feature of these alloys is their ability to form highly protective alumina scales at quite low N_{Al} levels. The oxide map in Fig. 7.20 shows that alloys containing more than about 20 wt% chromium require only 2–3 wt% aluminium to form $\alpha\text{-Al}_2\text{O}_3$. This is much less than the value of $N_{\text{Al}} > 0.14$ (ie, > 7.5 wt%) reported [32] for a binary alloy. Because the diffusion properties of the various oxides differ so much, oxidation rates vary strongly with alloy composition.

Fig. 7.21 compares the oxidation kinetics of several Fe-Cr-Al compositions with those of two sorts of Ni-Cr-Al alloys. The very rapid rates observed for

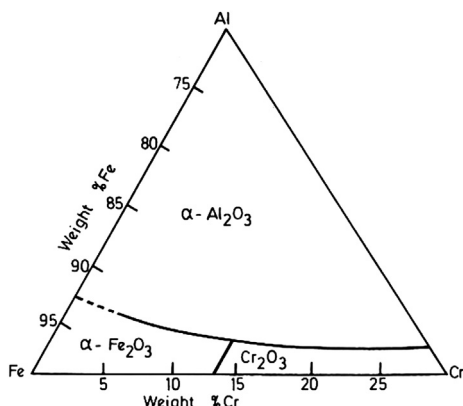


FIGURE 7.20 Oxide map for Fe-Cr-Al ternaries at temperatures greater than 1000°C [25].

dilute Fe-Cr-Al alloys correspond to growth of an iron-rich oxide layer above a layer of mixed oxides, and internal precipitation of aluminium and chromium-rich oxides. The intermediate curves were observed for high chromium and low aluminium levels. They represent growth of a chromia scale, interspersed with occasional iron-rich oxide modules. Depending on N_{Al} level, alumina precipitated internally or formed an almost continuous layer under the other oxides. The slow oxidation kinetics corresponded to alumina scale growth on alloys containing about 5 wt% aluminium. The two Ni-Cr-Al kinetic curves corresponded to chromia and alumina scaling.

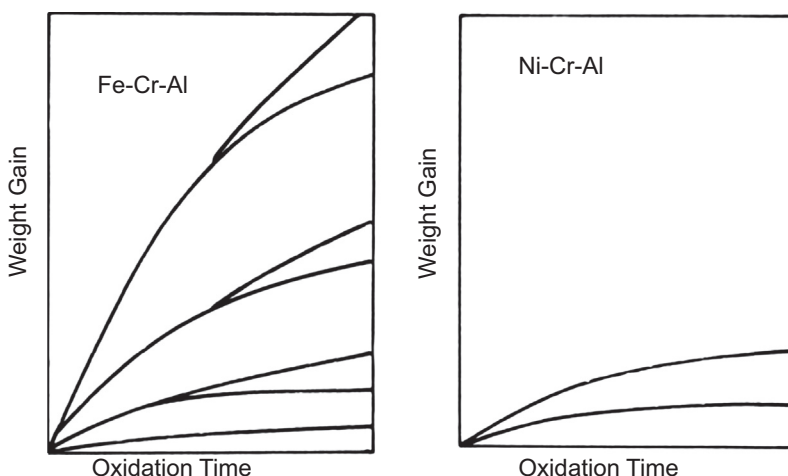


FIGURE 7.21 Relative oxidation rates of Fe-Cr-Al and Ni-Cr-Al alloys at 1000 and 1200°C. For identification of curves, see text. Published with permission from F.H. Stott, G.C. Wood, J. Stringer, *Oxid. Met.* 44 (1995) 113, © NACE International 1983.

The initial, transient oxidation of Fe-Cr-Al is similar to that of Ni-Cr-Al, although the establishment of a protective α -Al₂O₃ scale is easier on the former. Breakdown of the scales is more catastrophic for the iron-base alloys, simply because iron-rich oxides grow faster than their nickel equivalents. However, it is the lengthy period of steady-state oxidation following the initial transient which is of most interest. As is clear from Fig. 7.21 the establishment and maintenance of an alumina scale is essential for successful performance. It is therefore necessary to understand the mechanism whereby chromium additions reduce the value of $N_{\text{Al},\text{min}}$ required for alumina scale formation. This has come to be known as the ‘third element effect’ which is now discussed.

7.4.5 Third Element Effect

The third element in question is that component of a ternary alloy which forms an oxide of stability intermediate to those of the other two metals. Thus chromium is the third element in both Ni-Cr-Al and Fe-Cr-Al (Table 2.1). Wagner [93] examined early work [94,95] on the Cu-Zn-Al system and noted that ternary alloys formed protective Al₂O₃ scales at lower N_{Al} values than were required for Cu-Al binaries. He suggested that the explanation lay in the ability of zinc (the third element) to lower the oxygen activity at the scale-alloy interface.

Consider first a dilute binary Cu-Al alloy reacted at a high p_{O_2} so that Cu₂O grows in contact with the alloy. The value of a_{o} at the scale-metal interface is then set by the Cu/Cu₂O equilibrium which corresponds to $p_{\text{O}_2} = 10^{-10}$ atm at 850°C, the temperature of oxidation. Now consider the effect of adding to the alloy sufficient zinc to form a surface oxide layer. Because ZnO is more stable than Cu₂O, it is the former which develops at the scale-alloy interface, and p_{O_2} is now controlled by the Zn/ZnO equilibrium. Allowing for the low a_{Zn} value in the depleted alloy, we calculate from the thermodynamic data of Table 2.1 that $p_{\text{O}_2} \approx 10^{-21}$ atm. Recalling that the dissolved oxygen concentration is given by Sievert’s Eq. [2.71], it is seen that $N_{\text{o}}^{(\text{s})}$ in copper is 10⁵ times lower beneath a ZnO scale than one of Cu₂O. Accordingly, the balance between inward oxygen diffusion to cause internal aluminium oxidation and outward aluminium diffusion to form an external scale is altered (Eq. [7.5]), and protective scale formation is more favoured. It is recognised that for such a mechanism to function, the third element must have an oxide of intermediate stability, so that it displaces Cu₂O and lowers the interface p_{O_2} value but is not more stable than Al₂O₃. If it were more stable, it would form deep within the alloy or itself make up the most stable scale.

This model can be tested for the Ni-Cr-Al and Fe-Cr-Al systems, assuming that a transient chromia scale controls the alloy surface oxygen activity. If the residual a_{Cr} value is estimated as 0.1, then an equilibrium value of $p_{\text{O}_2} = 1.5 \times 10^{-15}$ atm is estimated for 1200°C. Evaluating the Sievert’s law constant from the data in Table 2.2, one calculates $N_{\text{o}}^{(\text{s})}$ equal to 2.2×10^{-7}

and 6.4×10^{-6} in nickel and ferritic iron, respectively. Substitution of these values into Eq. [7.5] along with estimates for D_O , D_{Al} then leads to $N_{Al,min}$ estimates of 0.005 in nickel-base alloys (0.3 wt%) and 0.002 in iron-base alloys (0.1 wt%). These values are certainly much lower than those calculated for binary alloys under Rhines pack conditions (Table 6.8). Unfortunately, they are unrealistic, being also much lower than the experimentally observed requirements, summarised in Figs. 7.20 and 7.22. At 1200°C, the results of Giggins and Pettit [91] showed that $N_{Al} = 0.035\text{--}0.11$ was required in the range $N_{Cr} = 0\text{--}0.4$.

As noted in Section 7.2, the establishment of a protective Al_2O_3 scale on binary alloys required N_{Al} to be high enough not only to avoid internal oxidation, but sufficient to ensure the scale was made up of alumina only, rather than a mixture of oxides. In a sense, the addition of chromium to the alloy achieves the same purpose of converting the scale from a multiphase reaction product to one of alumina only. A number of proposals have been advanced to account for this effect.

The presence of a third metal will inevitably alter the thermodynamics of the alloy sub-surface region, where the competition between different oxidation processes takes place. In principle, the activities and effective diffusion coefficients of all components -M, Cr, Al and O- will vary with composition (Section 2.7) and affect the competition between internal and external oxidation [96]. We have already seen that the addition of even the oxygen unreactive metal platinum plays an important role in its effect on a_{Al} . When the third element is reactive to oxygen, then it will obviously effect the activity, and hence solubility, of oxygen. The example of chromium additions decreasing $N_o^{(s)}$ in Ni-Al is shown in Fig. 6.41. Such an effect would decrease inward oxygen diffusion, lessening the likelihood of internal oxidation.

Ternary interactions between the two oxygen-reactive metals need also to be considered. Nesbitt [16] examined the effect of chromium additions on the

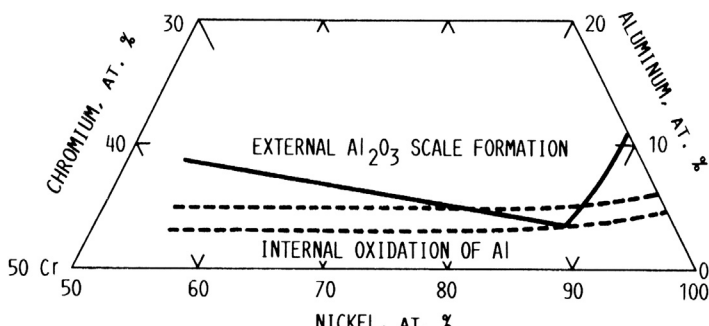


FIGURE 7.22 Minimum $N_{Al}^{(o)}$ for exclusive Al_2O_3 scale formation at 1200°C: continuous line measured [16], dashed lines calculated [16]. Reproduced by permission of The Electrochemical Society.

aluminium flux in oxidising Ni-Cr-Al alloys. Application of Eq. [2.115] to this system yields

$$J_{\text{Al}} = -D_{\text{Al Al}} \frac{\partial C_{\text{Al}}}{\partial x} - D_{\text{Al Cr}} \frac{\partial C_{\text{Cr}}}{\partial x} \quad [7.29]$$

and it is recognised that oxidation leads to a gradient in C_{Cr} in the same direction as that of C_{Al} . Measurements by Nesbitt and Heckel [97] showed that $D_{\text{Al Cr}}$ was positive and varied in magnitude with composition from 20% to 50% of $D_{\text{Al Al}}$ in the γ -phase at 1200°C. Thus the second term in Eq. [7.29] leads to an increase in J_{Al} , and one which can be substantial. Nesbitt [16] applied Eq. [7.29] to calculating the minimum value of $N_{\text{Al}}^{(o)}$ necessary to sustain growth of an external alumina scale, using Wagner's criterion Eq. [5.22]. The results of the calculation are compared with measured data [91] in Fig. 7.22, where agreement seems to be reasonable in the range $N_{\text{Cr}} = 0.05\text{--}0.20$. However, neither the D_{ij} nor k_c is particularly sensitive to N_{Cr} . The consequent insensitivity of $N_{\text{Al,min}}$ to the value of N_{Cr} indicates that the basic concept is inapplicable [16].

Zhang et al. [33] have pointed out that the transition involved in achieving exclusive alumina scaling of both Fe-Cr-Al and Ni-Cr-Al is one away from formation of a multiphase scale. Thus the third element effect envisaged by Wagner is not involved, as there is no internal oxidation except at very low $N_{\text{Al}}^{(o)}$ values. Applying a model proposed by Niu and Gesmundo [98], they suggest that the third element effect in M-Cr-Al systems is simply due to a destabilisation of the fast growing iron or nickel oxides as the value of N_{Cr} is increased. The effect is strong, because Cr_2O_3 and Al_2O_3 are completely miscible, and the presence of chromium increases the total concentration ($N_{\text{Cr},i} + N_{\text{Al},i}$) at the alloy-scale interface, promoting the formation of $(\text{Al,Cr})_2\text{O}_3$. No quantitative verification of this proposal is yet available.

It seems likely that the third element effect includes a number of factors which are simultaneously in operation. In addition to the thermodynamics and kinetic effects mentioned so far, it is also possible that the third element may, if dilute, oxidise internally, increasing the total volume of internal oxide, g , thereby promoting scale formation according to Eq. [7.5]. In this case, $(N_{\text{B,min}} + N_{\text{C,min}})$, and the right hand number of the equation becomes the sum of two terms for the two oxidising metals. Such an approach was suggested by Boggs [99] as a basis for Fe-Si-Al alloy development, and has been explored quantitatively by Niu et al. [13] for Ni-Si-Al alloys. In the latter case, the authors calculated that the value of $N_{\text{Al,min}}$ at 1000°C was reduced from 0.11 to 0.05, as N_{Si} was increased from zero to 0.065. This prediction was in accord with experimental results obtained by these authors and others [100–102] for dilute alloys. However, an alloy with $N_{\text{Si}} = 0.05$ and $N_{\text{Al}} = 0.20$ oxidised internally [103].

This last finding illustrates one aspect of the weakness of the usual diffusion models: they ignore microstructural effects, assuming that diffusion is always

via the alloy lattice, or its interstitial sites in the case of oxygen. As noted by Niu et al. [13] the internal precipitation of SiO_2 and Al_2O_3 is accompanied by very large volume changes and the formation of high dislocation densities. This favours rapid diffusion. Another factor is the frequent formation of aligned rod and lath shaped precipitates when aluminium and silicon oxidise internally (Fig. 6.32), and the resulting rapid diffusion of oxygen along the oxide-matrix interfaces. In short, the values used for D_o in Eq. [7.5] are inappropriately low. Similarly, effective values of D_B are enhanced if the alloy subsurface region is in a cold-worked condition before service.

A further weakness of the diffusion theory approach is its failure to deal with the kinetics of oxide nucleation and growth. As seen in Section 5.7, formation of Cr_2O_3 accelerates the rate at which the isomorphous and highly protective α -modification of Al_2O_3 is formed. The greater ease of α - Al_2O_3 formation on Fe-Cr-Al may reflect also a similar templating effect due to Fe_2O_3 . A detailed study of oxide nucleation and growth kinetics during the transient stages of M-Cr-Al oxidation reactions would be of value.

Although predictive capacity is limited, our empirical knowledge of the oxidation behaviour of M-Cr-Al alloys is sufficient to allow the identification of appropriate compositions for alumina formation. However, none of these ternary alloys will be of practical value, because the alumina scales are prone to spallation. This important defect and the means for its rectification are now considered.

7.5 SCALE SPALLATION

Alumina scales formed on both M-Al and M-Cr-Al spall when cooled from reaction temperature. The result of scale spallation is that oxidising gas gains access to a depleted alloy surface, which might not be able to reform protective oxide. As discussed in Section 2.10, stress in the scale-alloy system results from the differential thermal contraction of the metal and oxide on cooling. The stress can be rapidly induced and therefore cannot be relieved by time-dependent creep processes. Chromia scales also fail mechanically but appear to be less susceptible. This generalisation may reflect partly the different thermal expansion coefficients, with particularly low values for ferritic chromia formers (Table 2.4). Scale spallation, and also cracking, can sometimes occur during isothermal oxidation. These failures result from growth stresses rather than thermal ones, as discussed briefly in Section 2.10.

Scale failure occurs when the magnitude of the stress and/or the strain rate are too great for the scale-alloy system to accommodate by deformation. Factors affecting the initiation of failure therefore include the microstructure, defect size and frequency, and intrinsic mechanical properties of the oxide, the alloy and the interface between them [86,104,105]. The topic is a large one, and no attempt is made to deal with it here. Instead, attention is directed to the factors which differentiate spallation-prone and spallation-resistant systems.

A useful way of examining the factors contribution to scale spallation is provided by the techniques of fracture mechanics [106]. The energy released by the growth of an existing defect is compared with the work done in creating the new surfaces in, for example, extending a crack. When the energy released is large enough, the defect grows spontaneously. A major source of mechanical energy is the thermally induced stress resulting from rapid cooling after oxidation. The resulting stored elastic energy per unit area of scale-alloy interface, W^* , is written as

$$W^* = (1 - \nu_p)E_{\text{OX}}(\Delta T \Delta \alpha)^2 X \quad [7.30\text{a}]$$

and the associated elastic stress σ^*

$$\sigma^* = \left(\frac{W^* E_{\text{OX}}}{1 - \nu_p} \right)^{1/2} \quad [7.30\text{b}]$$

where the notation of Section 2.10 has been employed. Clearly, the energy available to cause mechanical damage to the scale increases with its thickness. Various modes of failure are possible and can be investigated using the basic result for linear plastic deformation that crack growth occurs when

$$\sigma_c f \sqrt{\pi a} > K_c \quad [7.31]$$

where σ_c is the critical stress required to cause crack growth, $2a$ the length of a defect (crack, void, etc.), f a numerical factor related to crack shape and precise failure mode and K_c a material property representing resistance to crack propagation. Larger values of a correspond to greater susceptibility to spallation.

7.5.1 The Sulphur Effect

The presence of sulphur as an alloy impurity is associated with a greater tendency to scale spallation. This is true not only for β -NiAl but also for M-Cr-Al alumina formers and a variety of chromia formers. This was made clear by the finding that ultra low (1 ppm) sulphur alloys evidenced much better scale retention than did the same alloys at normal sulphur levels of tens of ppm [74,107]. Smialek et al. [108–112] confirmed the conclusion by demonstrating that desulphurising alloys improved their alumina scale retention.

Several workers [70,71,108,113–115] have shown that sulphur from the alloy segregates to the scale-metal interface. Sigler [116] suggested that the sulphur weakens the interface in the same way as it embrittles metal grain boundaries. This would correspond to a decrease in K_{IC} in Eq. [7.31]. Another view developed by Grabke et al. [117–119] is that sulphur adsorbs on free metal surfaces within voids at the scale-alloy interface. This would stabilise the voids, permitting them to grow. This corresponds to an increase in a in Eq. [7.31], decreasing the critical stress required for spallation.

Other impurities such as carbon or nitrogen, have been suggested [116,120–122] as playing a role in scale adhesion. Alloy desulphurising treatments also remove carbon, so any carbon effect is masked in those experiments. However, experimental NiAl alloys with different Hf/C ratios [121] developed different degrees of convolution at their scale-alloy interfaces. When the Hf/C solute atom ratio was <1 , the degree of convolution increased, as did the extent of spallation. Presumably, this indicates that when insufficient hafnium is available to precipitate the carbon as HfC, the remaining carbon affects the interface. The mechanism of this interaction is not known.

7.5.2 Interfacial Voids and Scale Detachment

Voids at the scale-alloy interface or regions of scale detachment are examples of defects which can act as crack or spallation initiation sites. Their formation and growth are therefore likely preludes to scale failure. Possible explanations for such defects include vacancy injection into the alloy followed by coalescence at a suitable nucleation site, and Kirkendall porosity. Since $\alpha\text{-Al}_2\text{O}_3$ scales grow mainly by inward diffusion of oxygen along grain boundaries, as shown by $^{18}\text{O}_2$ tracer diffusion studies [123–125], the vacancy injection model appears to be inapplicable. As discussed in Section 5.8, the Kirkendall effect accounts satisfactorily for the interfacial voids formed at the $\beta\text{-NiAl}$ surface beneath an $\alpha\text{-Al}_2\text{O}_3$ scale. However, growth of the transient aluminas, which is much faster, may be supported by grain boundary cation diffusion [126,127]. Thus interfacial porosity could be developed during the initial transient reaction period, if it were long-lived, by vacancy injection. Chromia scales also grow by grain boundary diffusion (Sections 3.9 and 7.3), and $^{18}\text{O}_2$ tracer studies have shown that chromium is the principal differing species. In this case, void nucleation at the scale-metal interface might result from vacancy injection into the metal, their supersaturation and condensation at the interface.

Important features common to both Cr_2O_3 and $\alpha\text{-Al}_2\text{O}_3$ scale growth are the continuation of oxidation despite the presence of voids and the development of wrinkles in the oxide. The resulting scale appearance is shown schematically in Fig. 7.23. The scales continue to grow because the vapour pressures of chromium [128] and aluminium [129] are high enough to sustain the rather slow scale-thickening rates. A more interesting question concerns

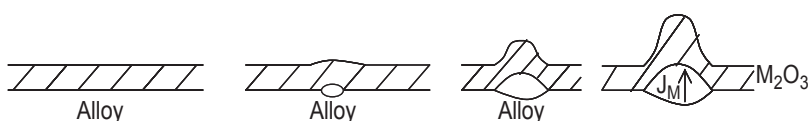


FIGURE 7.23 Detachment of scales and the development of wrinkles.

the driving force for wrinkle development and enlargement of the underlying voids. A frequently proposed explanation [86,126,130,131] is that of oxide formation within the scale interior, causing a compressive growth stress which is relieved by wrinkling. Such a mechanism was first proposed by Rhines and Wolf [132] to explain the development of compressive stress in growing NiO scales. For this to happen, it is clear that both metal and oxygen must be delivered to the growth locations in the scale interior.

As noted above, tracer diffusion measurements have shown that metal diffusion predominates in chromia growth whereas oxygen diffusion is the principal process in α -Al₂O₃ growth. However, they are not the only processes involved. In the case of chromia, tracer diffusion studies [133] show that there is also a contribution from inward oxygen diffusion. Similarly, α -Al₂O₃ scale growth involves the diffusion of metal as well as oxygen [123]. However, although mass transport of both species is evidently available, the mechanism whereby oxide precipitates within a matrix of the same oxide is not obvious. Indeed, it would be impossible if the diffusion species were lattice defects, in local equilibrium with each other via

$$a_M^2 a_O^3 = \exp[-\Delta G_f^\circ(M_2O_3)/RT] \quad [7.32]$$

together with defect reactions such as Eq. [3.123] and Eq. [7.8]. No mechanism for achieving the supersaturation necessary to precipitate new oxide is apparent in this case.

The necessary conditions for new oxide formation can be achieved at the scale-gas and scale-alloy interfaces. They might also be achievable at grain boundaries if the mobile species are not in strict local equilibrium with the adjacent oxide. As discussed in Section 4.4, chromia scales are permeable to molecular species such as N₂ and CO, presumably via grain boundary diffusion. Tracer diffusion measurements have shown [134] that H₂O also penetrates chromia scales. Thus it seems likely that the O₂ species can also enter the grain boundaries, enabling supersaturation with respect to Eq. [7.32] to occur.

The development of scale wrinkles (or ripples) need not lead to detachment if (a) no defects capable of acting as stress raisers are present, and (b) the alloy can deform to remain in contact with the elongated scale. The role of sulphur impurities in stabilising interfacial voids could therefore be important. Even in its absence, a rumpled interface develops local tensile stresses which might exceed the critical stress level necessary to create a void [135].

Most of the factors mentioned here as relevant to scale detachment and spallation are affected profoundly by the presence in the alloy of small concentrations of ‘reactive elements’, ie, metals with exceptionally strong affinity for oxygen, such as Hf, Ce, Y, La, etc.

7.5.3 Reactive Element Effects

An application of the reactive element effect (the addition of Ce to a Ni-Cr alloy) was patented by Pfeil [136] in 1937. Since then, reactive element additions have become a key part of high-temperature alloy design, supported by a very large research effort. Much of this activity has been reviewed by Stringer [138], Prescott and Graham [139], Whittle and Stringer [137] and more recently by Pint [47] and Chevalier et al. [140].

Reactive element additions improve greatly the ability of chromia and alumina forming alloys to resist scale spallation. Understanding this phenomenon has been made difficult by the multiplicity of effects reactive elements have on alloy-scale systems. The most obvious of these are the changes in scaling rate and mass transfer mechanisms.

Tracer diffusion studies with $^{18}\text{O}_2$ [124,133] showed that the addition of reactive elements to chromia-forming alloys slowed the diffusion of chromium through the scales. As a result, scale growth was due mainly to the inward diffusion of oxygen. Similar measurements on alumina formers [123,124,141–143] showed that the transport mechanism was changed from mixed oxygen and aluminium transport to principally oxygen transport when a reactive element was present. However, because $\alpha\text{-Al}_2\text{O}_3$ growth was in any case controlled by oxygen transport, the effect on the overall rate was less than in the chromia case. To the extent that oxide scales are made thinner, their susceptibility to spallation is predicted from Eq. [7.30] to be lessened.

Oxide microstructures are altered by the presence of reactive elements. Chromia scales become finer grained, with some increase in grain size in the growth direction, ie, toward the scale-metal interface [144–146]. Alumina scales are changed by reactive elements from coarse and equiaxed to fine and columnar [130,131,147]. An example of this effect is shown in Fig. 7.24.

The oxide-alloy interface is also altered by the presence of reactive elements. Sulphur segregation to this interface is found to be suppressed [125,131,147,148], wrinkling and scale detachment is decreased [115,130,149], oxide intrusions or ‘pegs’ in some cases grow into the alloy [136] and the interface is strengthened [75] in the case of a desulphurised alloy.

The ways in which this multitude of effects lead to the beneficial outcome of much reduced spallation have been the subject of considerable debate. However, recent advances in instrumentation have served to resolve a number of disputes. Auger electron spectroscopy experiments have proven that sulphur does indeed segregate to alloy-scale interfaces [115,117,150,151], and analytical TEM work [114,152] has shown that this occurs in regions of contact, not just in voids or cavities.

A series of scanning transmission electron microscopy studies has made clear that reactive elements segregate to oxide grain boundaries and have also been found at the scale-alloy interface [140]. It is the enrichment of reactive elements at oxide grain boundaries that alters their transport properties.

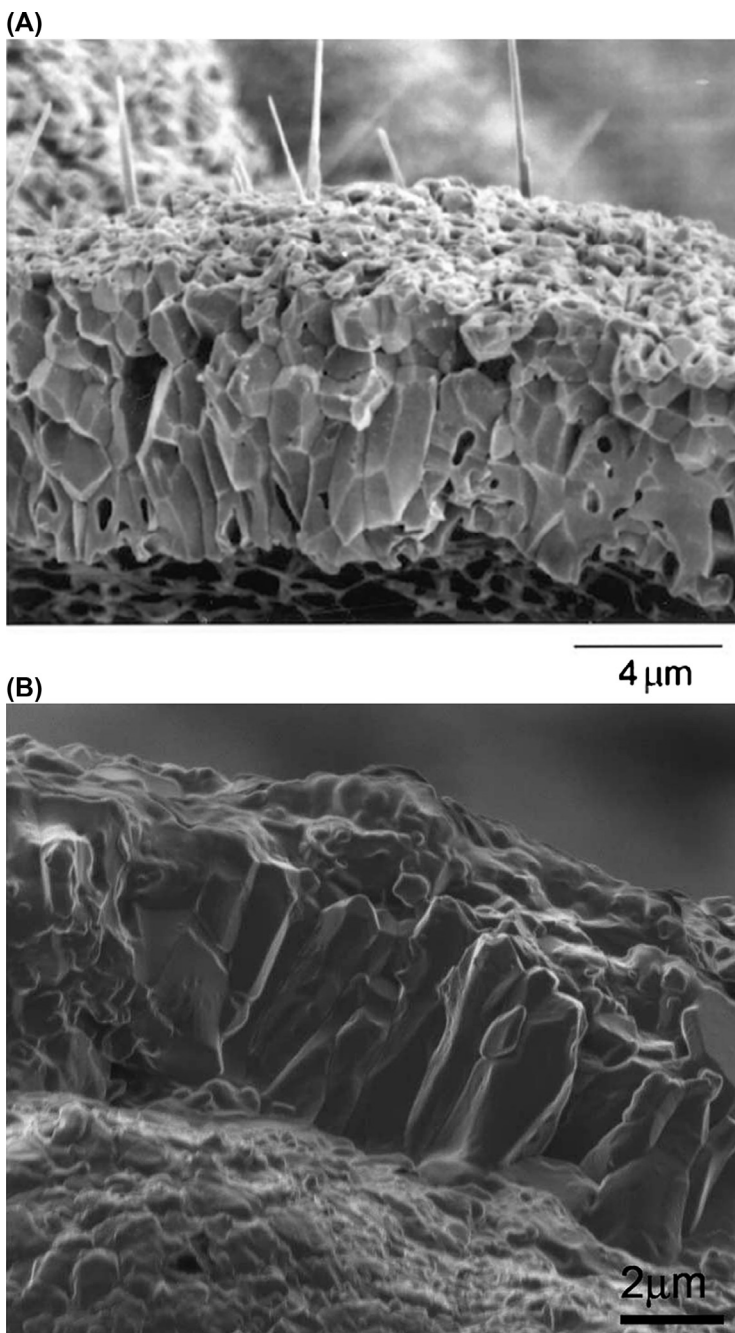


FIGURE 7.24 $\alpha\text{-Al}_2\text{O}_3$ scales grown at 1200°C on $\beta\text{-NiAl}$ (A) equiaxed oxide on undoped intermetallic and (B) columnar oxide on $\text{NiAl} + \text{Hf}$.

Reactive elements have a strong affinity for sulphur as well as oxygen. They are therefore able to desulphurise the alloy, forming sulphide or oxy-sulphide particles and preventing sulphur contamination of the scale-alloy interface. An alternative possibility is the preferential segregation of sulphur to surfaces of internal reactive element oxide particles. Removal of sulphur strengthens the scale-alloy interface, increasing its K_{IC} value and therefore increasing spallation resistance (Eq. [7.31]). In the absence of sulphur, nucleation of voids at this interface may also be more difficult.

Another factor improving scale adhesion is the greatly decreased extent of rumpling. This is attributed [86,125,131] to the reduction in growth stresses resulting from the fact that new oxide no longer forms within the scale when only one component diffuses. Of course this would not be relevant to the differential thermal contraction stresses generated during cooling. However, the reduced scale thickness is of benefit, as seen in Eq. [7.30]. Finally, it is to be observed that if reactive element additions favour inward oxygen diffusion, then oxide growth occurs at the scale-alloy interface, preventing the growth of voids there. In this case, a is very small, and according to Eq. [7.13], spallation resistance is enhanced.

Reactive elements also change the transient oxidation stage of reaction. Selective oxidation of chromium is promoted [153,154], perhaps nucleated by reactive element oxide particles [155]. In the case of alumina formers, much of the transient behaviour is associated with the rapid growth of metastable $\theta\text{-Al}_2\text{O}_3$, the transformation of which into the α -phase is discussed in Section 5.7. Unfortunately, there appears to be no single, unified description available for the effect of reactive elements on this transformation [140].

The various reactive elements differ in effectiveness in different alloy systems. An important factor is the limited solubility of these elements, which varies with both the identity of the additive and the nature of the solvent alloy. Excessive additions can lead to the precipitation of intermetallic phases which are susceptible to internal oxidation. The effects of a number of different additives on alumina scale performance on a variety of alloys have been reviewed by Hou [156].

7.6 EFFECTS OF MINOR ALLOYING ADDITIONS

A number of other elements are commonly present in heat-resisting alloys. These can derive from the processing operations used to manufacture the alloy, or can be deliberately added to enhance alloy properties. Examples of the former group are silicon, used to deoxidise steels, and manganese, used as a desulphuriser. Examples of the latter are titanium, added to steels as a carbide former and to superalloys as a γ' - $\text{Ni}_3(\text{Ti},\text{Al})$ former, and reactive elements. Minority element effects on chromia scaling have been reviewed by Gleeson and Harper [157], and for alumina scaling by Hou [156] and Pint et al. [158].

7.6.1 Silicon Effects

Because SiO_2 is less stable than Al_2O_3 (Table 2.1) but much more stable than FeO or NiO , it acts as a ‘third element’ in M-Si-Al alloys. However, silicon levels in commercial alumina-forming alloys are generally rather low, and this effect is not available. During steady-state alumina scale growth, silicon will remain unreacted in the alloy. Its role during the initial transient oxidation of alumina formers has not been studied.

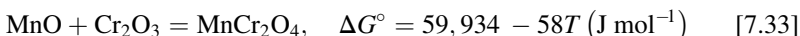
Silica is much more stable than Cr_2O_3 and forms beneath a chromia scale as internal precipitates (Fig. 5.1D) or, if $N_{\text{Si}}^{(o)}$ is high enough and sufficient time elapses, as a more-or-less continuous layer (Fig. 7.25). This layer is important in slowing the rate of chromia scale growth by acting as a partial barrier to diffusion [159–161]. In some cases [162,163] the silica layer was reported to be vitreous and hence a particularly effective diffusion barrier. It also provides additional protection against attack by carbon when the alloy is exposed to carburising-oxidising environments (Chapter 9). However, in the absence of reactive elements, the silica layer can make the scale more susceptible to spallation [164,165].

The transient oxidation of chromia formers is strongly affected by the presence of silicon, which promotes exclusive Cr_2O_3 formation. This is observed for iron-base [166,167], nickel-base [168] and cobalt-base [169,170] alloys and is generally thought to be a nucleation effect, although direct experimental evidence is lacking.

Silicon additions can also alter the diffusional properties of the alloy subsurface region. Johnston [171] examined diffusion in Ni-Cr-Si alloys and found that increasing silicon levels increased D_{Cr} by around 20%. Li and Gleeson [172] measured chromium depletion profiles in oxidised Ni-28Cr and Ni-28Cr-3Si, obtaining the results shown in Fig. 7.26. They deduced average values for the effective diffusion coefficient of chromium, which were increased by a factor of two in the presence of silicon, much greater than the effect reported by Johnston. No significant gradient in silicon developed, so no diffusional cross-effects were involved. An alternative explanation is that the formation of a SiO_2 layer [172] between the NiCrSi alloy and its chromia scale led to chromium diffusion being at least partly controlled by the silica, rather than by alloy diffusion.

7.6.2 Manganese Effects

The oxide MnO is more stable than Cr_2O_3 and might be expected on that basis to form a sublayer beneath a chromia scale. This does not in fact happen for several reasons. Firstly, the manganese spinel is stable with respect to the binary oxides [173].



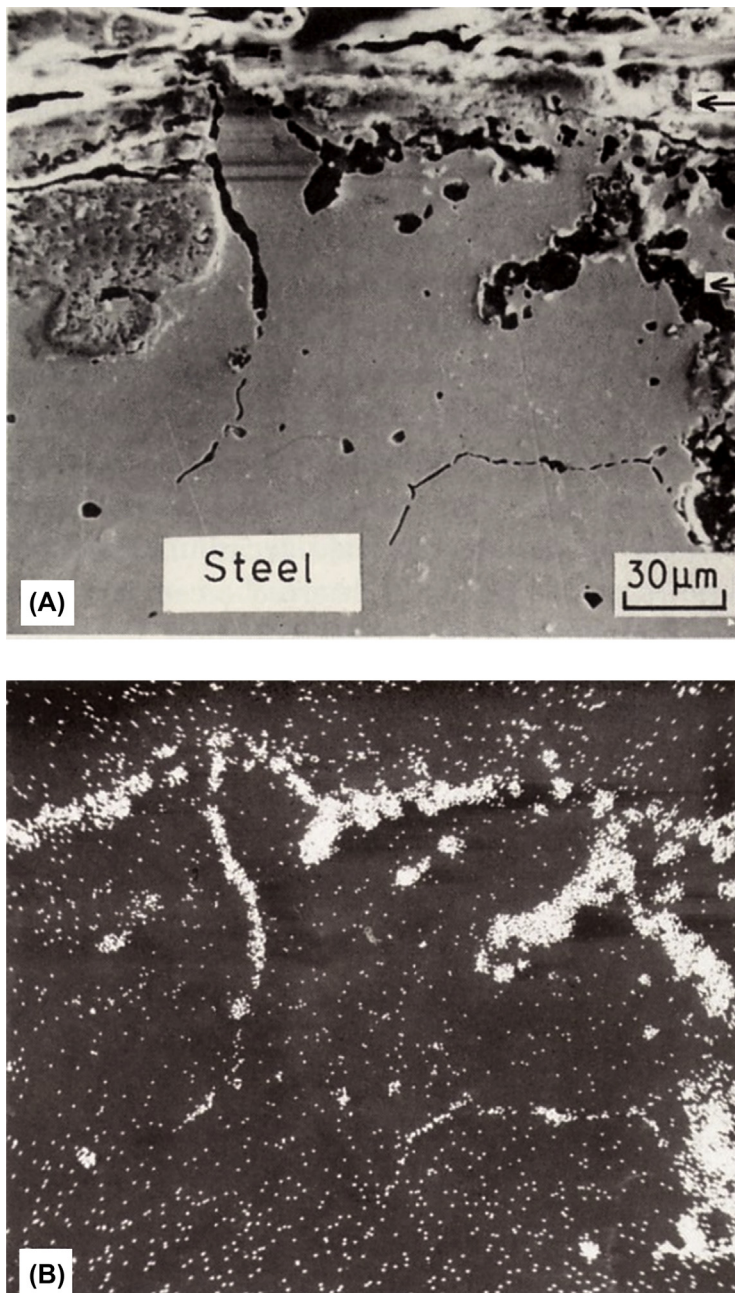


FIGURE 7.25 Oxidation of HK40 in steam cracking furnace: (A) SEM image (B) Si X-ray image. *With kind permission from M.J. Bennett, J.B. Price, J. Mater. Sci. 16 (1981) 170, Springer Science and Business Media.*

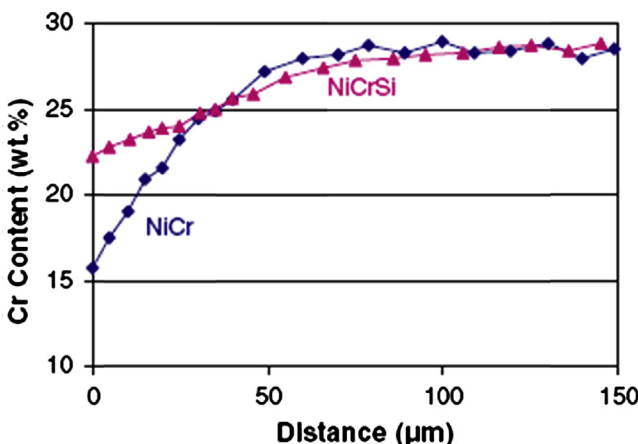
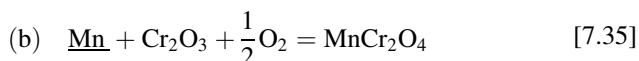
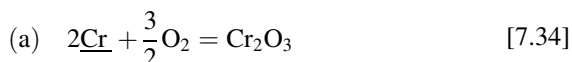


FIGURE 7.26 Subsurface depletion measured by EPMA in Ni-28Cr and Ni-28Cr-3Si after seven days oxidation in air at 1000°C. With kind permission from B. Li, B. Gleeson, *Oxid. Met.* 65 (2006) 101, Springer Science and Business Media.

Secondly, manganese is soluble in Cr_2O_3 , up to a limit of 1.6% of the cation sites at 1000°C [174]. Finally, manganese diffuses rapidly in Cr_2O_3 , apparently via the lattice rather than grain boundaries (Table 7.2), but relatively slowly in the alloy. This results in the scale structure of Fig. 5.1D.

This structure can be understood from the thermodynamics of the reactions



occurring on an MCrMn alloy. Assuming $a_{\text{Cr}} = 0.2$, one calculates from $\Delta G_f^\circ(\text{Cr}_2\text{O}_3)$ that $p_{\text{O}_2} = 2 \times 10^{-21}$ atm at the Cr_2O_3 -alloy interface for $T = 1000^\circ\text{C}$. From the value of $\Delta G_f^\circ(\text{MnO})$, it is found that MnO will form at this interface if $a_{\text{Mn}} > 2 \times 10^{-3}$. In a Ni-Mn alloy, this corresponds [175] to $N_{\text{Mn}} \approx 1 \times 10^{-2}$, a typical upper limit for many heat-resisting alloys. Given that the interfacial manganese concentration will be depleted below the bulk alloy value, the absence of MnO formation is readily understood.

As noted earlier, manganese diffuses rapidly through the chromia layer. Approximating its activity as being equal to that at the alloy surface, say $a_{\text{Mn}} \approx 1 \times 10^{-3}$, and assuming unit activity oxides, one calculates for reaction Eq. [7.35] the value $p_{\text{O}_2} = 1 \times 10^{-13}$ atm for the spinel-chromia interface. Thus the observed sequence of manganese spinel overlaying chromia in contact with the alloy is consistent with steady-state local equilibrium, despite the stability of the manganese oxides. At higher alloy manganese levels, spinel formation via reaction Eq. [7.35] can become favoured at the scale-alloy

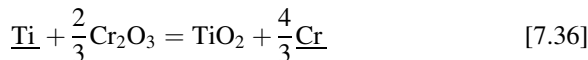
interface. Douglass and Armijo [164] reported that such a morphology developed on Ni-20Cr-3Mn at 1200°C.

Two-layered MnCr₂O₄-Cr₂O₃ scales are, of course, thicker than chromia scales and are consequently more prone to spallation [157]. They are commonly observed on stainless steels and cast heat-resistant steels [160].

7.6.3 Titanium Effects

Compared to chromium, titanium is a ‘reactive element’, forming TiO₂, which has a stability comparable to that of Al₂O₃. It also forms a very stable carbide and sulphide. In iron-based alumina forming alloys, titanium can function as a sulphur-getter. It has also been shown [143,146,147,158] to segregate to Al₂O₃ grain boundaries, where it may affect mass transfer. Diffusion of titanium along these boundaries to form titanium-rich oxides at the scale surface has been reported by Pint [131]. Finally, TiO₂ promotes the transformation of transient aluminas to α -Al₂O₃ (Section 5.6).

Some additional effects of titanium are observed in iron-based chromia formers. If TiC precipitates are present in quantity, their oxidation at locations where they intersect the surface causes a large volume change and disruption of the protective scale. Even if this effect is avoided, titanium decreases the oxidation resistance of chromia-forming alloys. It is reported [176,177] that the titanium oxidises both beneath the Cr₂O₃ scale and at its surface, indication that titanium can penetrate the chromia layer. The oxidation sites beneath the scale are intergranular, and may result from oxidation of prior carbides. Alloy solute titanium is presumably so dilute that TiO₂ cannot form via the reaction



Thus the situation is similar to that described earlier for low levels of manganese in chromia formers. The solubility of titanium in Cr₂O₃ has been measured by Naoumidis et al. [174] at up to 18% of the cation sublattice at 1000°C. Whilst no data are available for D_{Ti} in Cr₂O₃, the high concentrations of dissolved titanium suggest that lattice diffusion might account for the growth of outer titanium-rich oxides. Titanium also functions as a sulphur-getter in iron-based chromia-forming alloys [178].

7.6.4 Other Effects

Chromium can be present as a minority species in nickel-based alumina formers. At low concentrations, it does not provide a third element effect. Instead it is rejected from the alumina scale, concentrating at the scale-alloy interface [158,179]. In the case of β -NiAl, which has limited solubility for chromium (Fig. 5.36), α -Cr precipitates at the interface. The observed increase in scale spallation was attributed to the low thermal expansion coefficient of the α -Cr. A simultaneous increase in scale growth rate was unexplained.

Alumina scales are often found to contain small amounts of the alloy-base metal (usually iron or nickel). This is due to the initial transient oxide, which contains iron or nickel as a major component, being incorporated into the subsequently established alumina scale. As the alumina thickens, the overall concentration of alloy-base metal in the scale decreases but is not eliminated [156,180]. Analytical transmission electron microscopy has shown that the iron segregates to the grain boundaries [180], a finding confirmed by EELS analysis [181].

Hou [156] investigated the possible effects of this segregation on mass transport which, in $\alpha\text{-Al}_2\text{O}_3$ scales, is predominantly a grain boundary phenomenon. The resulting comparison for various alloys is shown in Fig. 7.27. Despite the scatter, it was possible to conclude that nickel and iron-based alloys reacted about 8 and 10 times faster than PtAl. The presence of chromium appeared to make no difference. Thus it appears that iron and nickel at alumina grain boundaries do affect their transport properties.

Chromia scales also contain small amounts of iron or nickel. However, there appears to be no direct information on possible segregation of these or other such metals to the oxide grain boundaries.

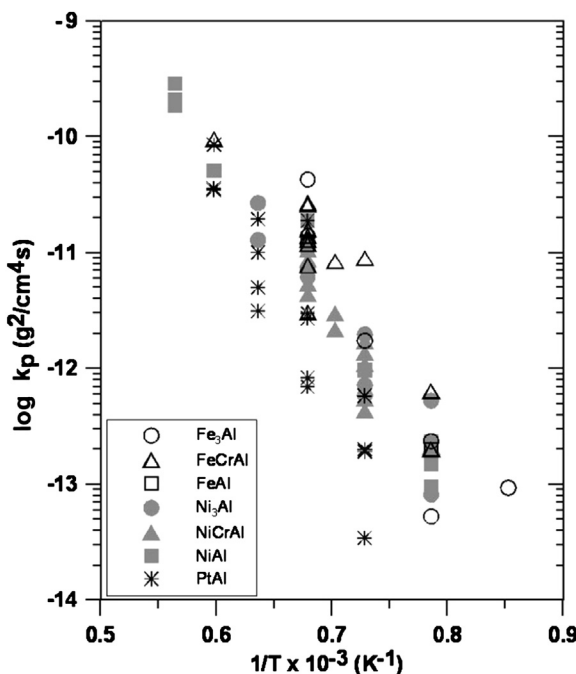


FIGURE 7.27 Oxidation rates for Al_2O_3 scale growth on Fe-, Ni- and Pt-based alloys. Published with permission from P.Y. Hou, *J. Am. Ceram. Soc.* 86 (2003) 660, the American Ceramic Society.

Finally, it is noted that the beneficial effects of platinum are also available from at least some other platinum group metals. Oquab and Monceau [182] have shown that palladium suppresses cavity formation at the alumina- β -NiAl interface. Similar benefits have been found for the addition of iridium [183] to γ/γ' -Ni-Al alloys.

7.7 EFFECTS OF SECONDARY OXIDANTS

Industrial gases commonly contain other reactants in addition to oxygen, those of principal concern being carbon and sulphur. Attack by these species will be discussed more fully in chapters 8 and 9, and our focus here is on the ability of chromia and alumina scales to resist them. In view of the fact that diffusion in these scales is principally via their grain boundaries, it is expected that these would be the sites most vulnerable to attack by foreign species.

It was seen in Section 4.4 that chromia scales grown on pure chromium could be penetrated by each of CO, SO₂ and N₂ under particular circumstances. Moreover, it was concluded on the basis of interactions among the different reactants that molecular species adsorbed on grain boundaries and were mobile to different extents within them. Such a mechanism has been confirmed in the case of H₂O by tracer diffusion measurements [134]. As we have seen, other alloy components can segregate to chromia scale grain boundaries and, at least in the case of reactive elements, alter their diffusion properties. The question of practical interest is therefore whether or not this segregation affects the permeability of the scale to secondary corrodents. It turns out that the answer to this question depends on both alloy composition and the gas atmosphere in question.

Fujü and Meussner [184] reacted Fe-Cr alloys containing up to 20 wt% Cr with pure CO₂ at temperatures of 700–1100°C and found that protective scales were never formed. Instead, chromium-rich carbides were internally precipitated, and the iron-plus-carbide surface oxidised to yield a two-phase inner layer of wüstite and iron chromium spinel. This was overgrown by an iron oxide outer layer, the constitution of which varied with temperature. This reaction morphology is consistent with the thermodynamics of the system. As oxygen activity decreases within the scale, the CO/CO₂ ratio increases according to Eq. [4.30], and the value of a_c rises according to Eq. [4.31]. A schematic view of the resulting profiles is shown in Fig. 7.28. Precipitation of the alloy chromium as carbide immobilises it and prevents the alloy forming a protective chromia scale. Higher alloy chromium levels, together with measures such as cold-working the surface, promote chromia scale formation, and much better protection against carbon attack is then available.

Colwell and Rapp [185] reacted Fe-24 Cr with CO₂/CO gases at 950°C, producing a chromia scale plus a limited amount of internal carburisation. However, they also found that Ni-Cr alloys with sufficient chromium to form an external scale were not carburised. The slightly richer alloys Fe-28 Cr and

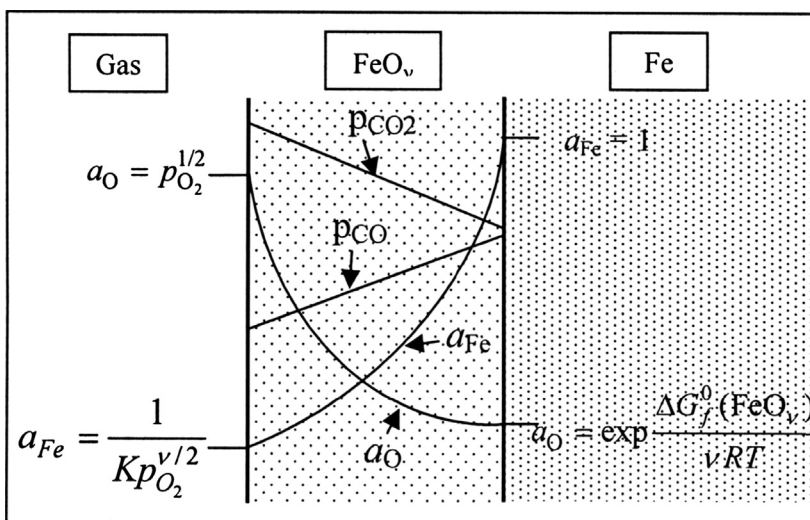


FIGURE 7.28 Variation of p_{CO_2} and p_{CO} in local equilibrium with oxygen gradient in a growing scale containing carbon.

Ni-28 Cr [186] developed chromia scales at 900°C in $CO_2/CO/N_2$ gas and were not carburised. Results obtained for stainless [187,188] and heat-resisting steels [189,190] are difficult to interpret because of the effects of other alloy components. The role of silicon in forming a SiO_2 scale sublayer (see Section 7.6.1) is particularly important and makes assessment of the chromia permeability impossible. A detailed account of corrosion by CO_2 is given in Chapter 10.

The carbon permeability of oxide scales on M-Cr chromia formers is much less than that of the scale on pure chromium (Section 4.4). Alteration of the grain boundary properties, perhaps by segregation of iron or nickel, evidently makes them less permeable to carbon. A possible mechanism is adsorption and immobilisation of CO or CO_2 on nickel or iron enriched surfaces, at oxygen potentials too low to form FeO . The effects of SO_2 additions to the CO/CO_2 gas also differ according to whether the scale is grown on chromium metal or an M-Cr alloy [191,192]. Carbon permeability through pure Cr_2O_3 was decreased, even at p_{SO_2} values too low to form an external scale. In contrast the carbon permeability of alloy scales was increased by the SO_2 additions, and internal carburisation followed. Sulphur adsorption on iron-enriched grain boundaries could prevent CO adsorption at these sites, allowing CO to penetrate the scale.

The situation in these gas mixtures is complicated still further by the permeability of chromia to sulphur [191,193]. Using radiotracer $H_2^{35}S$, Lobnig and Grabke [193] showed that the solubility of sulphur in sintered Cr_2O_3 was below the detectability limit of 0.1 ppm. Nonetheless, they found

that sulphur penetrated chromia scales, concluding that a molecular species was involved.

Alumina scales appear to be superior to chromia in their ability to exclude sulphur and carbon. Stott et al. [194] compared the resistance to sulphur of alumina scales on Fe-Cr-Al alloys with that of chromia scales on Fe-Cr materials by exposing them to H₂S/H₂O mixtures at 750°C. In both cases, sulphides formed as iron-rich nodules on the scale surface and also beneath the oxide scale as a result of sulphur penetration. Alumina scales resisted both forms of attack for longer than chromia, providing that scale cracking was avoided. Similar conclusions were reached by Sheybany and Douglass [195] for a variety of iron, nickel and cobalt-base alloys. Alumina scales are also superior to chromia in their ability to slow or prevent carburisation of cast heat-resisting alloys [196].

Several investigations of Fe-Cr-Al alloys [197–199] showed that sulphur penetrated α -Al₂O₃ scales at local sites. The ease of penetration increased at lower temperatures and decreased as scale adhesion was improved by alloy doping. Excessive amounts of yttrium caused precipitation of Fe-Y intermetallic particles [199], and more rapid attack occurred at sites where these intersected the surface.

The limited results available for alumina scales are consistent with the hypothesis that secondary corrodents can gain access to the underlying alloy by oxide grain boundary penetration. However, this process is slow and may be less important than mechanical failures such as cracking and spallation.

7.8 'AVAILABLE SPACE' MODEL FOR DUPLEX OXIDE SCALE GROWTH

Certain features of the development of duplex oxide scales by ferritic and ferritic-martensitic steels have led to the proposal of the ‘available space’ model. When these steels are corroded by compound oxidants such as CO₂ or H₂O, they grow two-layered oxide scales consisting of an outer zone of essentially pure iron oxide and an inner oxide zone containing most alloy components. This inner zone is commonly multiphase, fine-grained and porous (Figs. 10.4 and 11.18), with chromium present as spinel, Fe(Fe_{1-x}Cr_x)₂O₄. The thickness ratio for the two zones is constant, the interface between them being stationary with time and located at the prior surface of the steel.

Elements of the reaction mechanism were established long ago. Inert marker experiments [200] showed that the outer iron oxide grew outwards, and the inner zone grew into the metal. Scaling kinetics are parabolic, and the activation energy is consistent with grain boundary diffusion by iron [201]. This clearly accounts for the outward growth of iron oxide. On the other hand, oxygen transport required for the inward growth of the inner layer cannot possibly occur via solid-state diffusion, which is far too slow. The alternative possibility is molecular transport via rapid diffusion pathways of some sort.

Partial pressures of oxygen within the scale are very low (Sections 2.9 and 11.4) and cannot provide sufficient mass transport. However, either CO₂ or H₂O could easily supply sufficient oxygen transport to support inward growth of the inner scale layer. Evidence for such a mechanism is provided by the observation that either carbon or hydrogen is simultaneously injected into the steel. Thus chromium steels are found to simultaneously carburise whilst oxidising in CO₂ (see Section 10.2). Similarly, it is found [202] that substantial amounts of hydrogen are released from the outside of a steel tube being corroded on its inner surface by steam.

Final proof is provided by isotope experiments. Sequential exposure of a 9Cr steel to C¹⁶O₂ followed by C¹⁸O₂ led to the finding that ¹⁸O was enriched at the scale-alloy interface [203]. Similarly, exposure of P91 steel to N₂-¹⁶O₂-H₂¹⁸O [49] led to incorporation of the water molecule derived ¹⁸O in the scale interior. As noted by Rouillard et al. [204] and Martinelli et al. [205], the thickness ratio between inner and outer oxide scale layers grown on P91 steel is the same when grown in CO₂ or H₂O or even in liquid Pb-Bi containing dissolved oxygen. Moreover, the overall scale thickening rates at a given temperature are closely similar for P91 steel in all three environments. These observations are consistent with fast inward transport of the oxygen-carrying species in each case, and overall rate control due to outward iron diffusion.

Two related questions concerning this mechanism have attracted the attention of a number of authors [202,204–209]: firstly, just how new oxide is formed at the scale-alloy interface and what controls the rate when the oxygen supply is abundant, and secondly, how the volume of new oxide formed at this interface is accommodated. The general approach has been to recognise that newly formed oxide occupies space, and that metal consumption makes space available. The latter process is envisaged as the injection of vacancies into the alloy as metal atoms are removed into the oxide, followed by the condensation of at least some of these vacancies as voids at the scale-alloy interface. Gas access to the metal bordering a void then leads to further oxide formation.

Of course, the very same processes of metal consumption and its replacement by a larger volume of oxide occur in the oxidation of pure metals. The possibility of scale-metal separation and growth of porous oxide by gas-phase transport was recognised long ago by Pfeil [210] and Dravnieks and McDonald [211] in considering oxidation of pure metals. These ideas were developed by Bruckman and Romanski [212] and Mrowec et al. [213,214] into their dissociation model (Section 3.9.3), in which gaseous oxidant is released into a cavity at the scale-metal interface and oxidises the underlying metal.

This process was first described for the case of alloy oxidation by Gibbs [207], in terms of the vacancy volume made available, and subsequently by Robertson and Manning [209] as the available space model.

According to this model, the process limiting the rate at which the inner, chromium-bearing oxide layer grows into the alloy is the baring of oxidisable metal made available by void formation. Oxidation of such surfaces blocks gas

access, preventing further reaction until new voids are formed. Void formation results from vacancy injection accompanying outward diffusion of metal through the scale. Thus the answer to the kinetic question is that the rate of inward scale growth is controlled by solid-state diffusion in the scale.

The question of oxide volume accommodation at the scale-alloy interface has a similar answer. New oxide can form only as metal diffuses outward (to grow an outer scale layer) and removes material from the inner layer. The observation that the inner layer occupies the space corresponding to the alloy consumption zone reflects the fact that chromium is immobile, remaining in essentially the same position within the oxide as it formerly occupied in the alloy. The fixed ratio between inner and outer layer thicknesses results simply from conservation of mass, as the ratio of iron to chromium in the scale is the same as that in the alloy at modest temperatures where alloy diffusion is negligible. The questions of interest concern the reasons for the development of these poorly protective scale morphologies.

Whereas the P91 steel at temperatures around 600°C develops the classic thick scale morphology of outer iron oxide and inner chromium-bearing oxide in CO₂ (Fig. 10.4) and H₂O (Fig. 11.18), it forms a thin, protective, chromium-rich scale in air (Fig. 11.1). One reason for the difference has been noted above: much higher partial pressures of CO₂ or H₂O than O₂ are available within oxide scales and can support mass transport within pores so that inward scale growth becomes possible. The nature of the alloy is also important to pore formation, and a comparison with the behaviour of pure metals is useful.

Dravnieks and McDonald [211] proposed that development of a porous oxide layer to fill the space formerly occupied by metal would always occur. However, this is clearly not correct. For example, pure iron exposed to H₂/H₂O mixtures [215] or CO₂ [216] at high temperatures forms scales of dense oxide. Scaling rates are rapid, causing considerable metal surface recession, but no voidage or porosity is created at or near the oxide-metal interface despite the availability of H₂O or CO₂. Pure nickel also forms dense oxide, although the presence of low impurity levels, such as 0.1% chromium, leads to formation of an inner, porous oxide layer [201]. Both nickel and iron oxide grow by outward metal diffusion, corresponding to inward cation vacancy movement. If the oxide scales were rigid and unable to conform to the changing position of a receding metal surface, arrival of cation vacancies at this surface would generate free volume, ie, pores or voids. However, pure metal oxides are relatively plastic, particularly at high temperatures, and simply flow at the interface to retain contact with the metal. Arriving vacancies are then eliminated by the sweeping of atomic ledges across the metal surface.

This process of vacancy annihilation is analogous to that which occurs in a single-phase diffusion couple (Section 2.7.2). In the latter case, component flux imbalances lead to a movement of the entire lattice in the affected zone, in the process known as Kirkendall drift, and surplus vacancies are eliminated by

dislocation motion. When a metal oxide scale grows by outward cation diffusion and solid-state diffusion of oxygen is negligible, the flux imbalance can be compensated by movement of the oxide lattice and elimination of the vacancies at the scale-metal interface. The question of practical interest therefore concerns whether vacancies are disposed of at this interface or whether they form Kirkendall voids.

When other metals are present in an alloy, they can form second-phase oxides if unable to dissolve in the base-metal oxide. These particles impede plastic flow, leading to the appearance of voids and the onset of inward oxygen transport. At a macroscopic level, this explains the phenomenology of duplex layer growth. At an atomistic level, the scale-alloy interface is treated as a set of jogs and ledges, at which vacancies can be destroyed by jog and ledge movement [209]. In the case of pure metals, movement of these defects is relatively free. In the case of alloys, however, solute species can impede defect movement on the interface, preventing their operation as vacancy sinks. In this event, the vacancies can precipitate at the interface or within the substrate alloy [217]. Another possible fate for injected vacancies is that they annihilate within the alloy at sites where internal oxide precipitates nucleate and grow (Section 6.13).

The conditions for development of the duplex morphology (and relatively poor protection) are the presence of oxygen-bearing heteronuclear molecules, the existence of a mechanism limiting oxide plasticity and an inability of the alloy to supply sufficient chromium to support its selective oxidation. The latter can be remedied by the selection of higher alloy materials, appropriate to the service temperature. In situations where the duplex morphology cannot be avoided, oxidation rates can in principle be predicted on the basis of oxide grain boundary diffusion of iron.

7.9 STATUS OF MULTIPHASE SCALE GROWTH THEORY

From a practical point of view, the value of this theory lies mainly in its ability to guide alloy design or selection by showing how multiphase scales can be avoided, and a single-phase scale of the desired protective oxide arrived at. In this chapter, we have focused on chromia- and alumina-forming alloys, discovering that the more complex the reacting system, the weaker the theory.

For binary alloys, the treatment extends that of Chapters 5 and 6, which dealt with the situation where only one oxide was thermodynamically stable. Local equilibrium and the diffusion path description are found to apply equally well to the more complex case, where oxides of different metals form layers of a scale. Providing that adequate data are available, predictions as to whether the most stable oxide forms internally or as the desired scale are reasonably successful. However, marginal alloys can fail to maintain a steady-state condition, apparently as a result of changing mass transport mechanisms in the

scale. These changes can result from slow dissolution of the alloy solvent metal into the scale, or from mechanical damage.

A crucial factor in the design or selection of high-temperature alloys is the specification of a sufficient, but not excessive, level of chromium or aluminium. Not only must the level be high enough to prevent internal oxidation, but it must also suffice to sustain preferential growth of the desired scale. The critical concentrations are calculated from Eqs. [7.6] and [5.22], respectively. It is essential when performing these calculations to use k_p values appropriate for the actual gas to which the alloy will be exposed. Chromia scaling is often faster in CO_2 or H_2O than in oxygen, leading through Eq. [5.22] to a higher N_{Cr} requirement. Similarly, activation energies for scaling can differ with the oxidising gas species, leading to different $N_{\text{Cr,crit}}$ temperature dependencies.

Critical alloy concentrations required to avoid internal oxidation depend on temperature according to Eq. [7.6]. The corresponding expression for maintaining continuous scale growth is

$$R \frac{\partial \ln N_{\text{B,crit}}}{\partial (1/T)} = \frac{Q_{\text{B}} - E_{\text{A}}}{2} \quad [7.37]$$

Because $Q_{\text{B}} > E_{\text{A}}$ for ferritic chromia-forming steels in $\text{H}_2/\text{H}_2\text{O}$ atmospheres [218], $N_{\text{Cr,crit}}$ is predicted to decrease as the temperature increases. As a result, a given steel can passivate successfully at high temperatures (Region III in Fig. 7.29) but fail at the low temperatures of Region I. This results from the low value of $E_{\text{A}} = 110 \text{ kJ mol}^{-1}$ for this steel in $\text{H}_2/\text{H}_2\text{O}$ gas. In contrast,

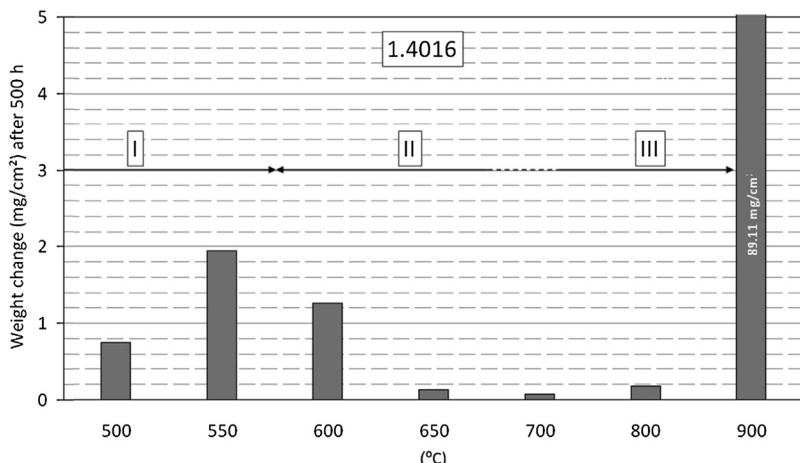


FIGURE 7.29 Temperature effects on weight uptake by ferritic steel 1.4016 (16.3 Cr, 0.19 Mn, 0.25 Si, 0.02 Al, 0.01 Ti) reacted for 500 h in Ar-4% H_2 -20% H_2O . Reprinted from D.J. Young, J. Zurek, L. Singheiser, W.J. Quadakkers, Corros. Sci. 53 (2011) 2131, with permission from Elsevier.

reaction in oxygen is characterised by higher activation energies ($\sim 230 \text{ kJ mol}^{-1}$), leading to a negative value of the right-hand member of Eq. [7.35], and the prediction that $N_{\text{Cr,crit}}$ increases with temperature.

At higher temperatures, the requirements of Eq. [7.5] must be met, and $N_{\text{Cr,crit}}$ is predicted [218] from an evaluation of Eq. [7.6] to increase with temperature. At a level of 16.3%, the steel of Fig. 7.29 had sufficient chromium to achieve protection at 700 and 800°C, but at 900°C, this concentration was insufficient, and oxidation in $\text{H}_2/\text{H}_2\text{O}$ led to breakaway. This is due to the greater temperature sensitivity of oxygen permeability, in ferrite equilibrated with FeO , over that of substitutional diffusion in the alloy.

Ternary alloys were found to pose a much more difficult problem, simply because data on oxygen solubility and diffusivity are so scant. Even in the case where the third metal is unreactive or only slightly reactive, its effects can be dramatic. The addition of platinum modifies the behaviour of nickel aluminides through thermodynamic interactions which reduce a_{Al} and lower oxygen permeability. Adding nickel to Fe-Cr has the principal effect of altering metal solubilities in the chromia scale. In the absence of good data for the effects on oxygen dissolution and diffusion, the changing patterns of reaction products are best described by oxide mapping. The Fe-Ni-Cr system is the basis for many heat-resisting alloys, and the consequently large body of descriptive data is the main support for oxidation resistant alloy design. Good-quality data for oxygen dissolution and diffusion in this system would be valuable.

Ternary M-Cr-Al alloys, with two reactive components, are the basis for many commercial compositions. The third-element theory developed to explain the effect of chromium in reducing the levels of aluminium required to form an external scale is only qualitatively successful. This appears to be due to the strong but unquantified thermodynamic interactions between dissolved oxygen and solute metals, and perhaps also to our weak understanding of the nucleation and growth phenomena of importance during initial transient oxidation.

Despite these limitations, our ability to achieve protective chromia or alumina formation by alloying is a practical reality. For these scales to be useful, however, they must be protected against cracking and spallation. This too can be achieved by reducing alloy sulfur levels, alloying platinum group metals with nickel aluminides and, most commonly, by alloying with reactive element metals. The rather complex range of effects induced by these additions can be understood from a simple view of the fracture mechanics of scale failure. However, quantitative alloy design tools for reactive element doping are not yet available.

The results surveyed in this chapter have reinforced our perception of the importance of oxide grain boundaries in the behaviour of chromia and alumina scales. In addition to providing the main pathways for diffusion of the chromia and alumina-forming species, they provide sites for reactive element

segregation, access points for other gas species such as N₂ and H₂O and probably preferred diffusion paths for alloy iron and nickel. We will return to this point in Chapter 11, but note that a quantitative knowledge of these processes would be highly desirable.

REFERENCES

- [1] C. Wagner, J. Electrochem. Soc. 103 (1956) 571.
- [2] C. Wagner, J. Electrochem. Soc. 103 (1956) 627.
- [3] C. Wagner, J. Electrochem. Soc. 99 (1952) 369.
- [4] C. Wagner, Z. Elektrochem. 63 (1959) 772.
- [5] B.D. Bastow, G.C. Wood, D.P. Whittle, Oxid. Met. 16 (1981) 1.
- [6] D.P. Whittle, in: R.A. Rapp (Ed.), High Temperature Corrosion, NACE, Houston, TX, 1983, p. 171.
- [7] D.L. Douglass, in: O. Johansen, A.G. Andersen (Eds.), Selected Topics in High Temperature Chemistry – Defect Chemistry of Solids, Elsevier, Amsterdam, 1989, p. 185.
- [8] F.S. Pettit, Trans. AIME 239 (1967) 1296.
- [9] H.M. Hindam, W.W. Smeltzer, J. Electrochem. Soc. 127 (1980) 1622.
- [10] W.W. Smeltzer, H.M. Hindam, F.A. Elrefaei, High Temperature Corrosion, NACE, Houston, TX, 1983, p. 251.
- [11] H.M. Hindam, D.P. Whittle, J. Mater. Sci. 18 (1983) 1389.
- [12] G.C. Wood, F.H. Stott, Br. Corros. J. 6 (1971) 247.
- [13] Y. Niu, Y. Wu, F. Gesmundo, Corros. Sci. 48 (2006) 1.
- [14] S. Hayashi, S. Narita, T. Narita, Oxid. Met. 66 (2006) 191.
- [15] F. Elrefaei, W.W. Smeltzer, J. Electrochem. Soc. 128 (1981) 2237.
- [16] J.A. Nesbitt, J. Electrochem. Soc. 136 (1989) 1511.
- [17] K. Hirano, A. Hishimima, J. Jpn. Inst. Met. 32 (1968) 516.
- [18] A.E. Paladino, W.D. Kingery, J. Chem. Phys. 37 (1962) 957.
- [19] Y. Oishi, W.D. Kingery, J. Chem. Phys. 33 (1960) 480.
- [20] H. Hindam, D.P. Whittle, Oxid. Met. 18 (1982) 245.
- [21] L.M. Atlas, W.K. Susnida, J. Am. Ceram. Soc. 41 (1958) 150.
- [22] J.A. Imlach, F.F. Glasser, Trans. J. Br. Ceram. Soc. 70 (1971) 227.
- [23] J.L. Meijering, Acta Met. 3 (1955) 157.
- [24] A.K. Stewart, M.T. Hepsworth, Trans. AIME 242 (1968) 698.
- [25] P. Tomaszewicz, G.R. Wallwork, Rev. High Temp. Mater. 4 (1978) 75.
- [26] W.E. Boggs, J. Electrochem. Soc. 118 (1971) 906.
- [27] P. Tomaszewicz, G.R. Wallwork, Oxid. Met. 19 (1983) 165.
- [28] W.W. Smeltzer, P.R.S. Jackson, H.A. Ahmed, in: G. Simkovich, V.S. Stubican (Eds.), Transport in Nonstoichiometric Compounds, Plenum Press, New York, 1983, p. 481.
- [29] A. Ahmed, W.W. Smeltzer, J. Electrochem. Soc. 133 (1986) 212.
- [30] J. Takada, S. Yamamoto, S. Kikuchi, Oxid. Met. 25 (1986) 93.
- [31] R. Prescott, M.J. Graham, Oxid. Met. 38 (1992) 73.
- [32] B.A. Pint, J. Leibowitz, J.H. De Van, Oxid. Met. 51 (1999) 181.
- [33] Z.G. Zhang, F. Gesmundo, P.Y. Hou, Y. Niu, Corros. Sci. 48 (2006) 741.
- [34] F.H. Stott, G.C. Wood, M.G. Hobby, Oxid. Met. 3 (1971) 103.
- [35] A.H. Heuer, J. Eur. Ceram. Soc. 28 (2008) 1495.
- [36] A.H. Heuer, D.B. Hovis, J.L. Smialek, B. Gleeson, J. Am. Ceram. Soc. 94 (2011) S146.

- [37] A.H. Heuer, T. Nakagawa, M.Z. Azar, D.B. Hovis, J.L. Smialek, B. Gleeson, N.D.M. Hine, H. Guhl, H.-S. Lee, P. Tangney, W.M.C. Foulkes, M.W. Finnis, *Acta Mater.* 61 (2013) 6670.
- [38] S. Kitaoka, T. Matsudaira, M. Wada, *Mater. Trans.* 50 (2009) 1023.
- [39] T. Matsudaira, M. Wada, T. Saitoh, S. Kitaoka, *Acta Mater.* 58 (2010) 1544.
- [40] M. Wada, T. Matsudaira, S. Kitaoka, *J. Ceram. Soc. Jpn.* 119 (2011) 832.
- [41] T. Matsudaira, M. Wada, T. Saitoh, S. Kitaoka, *Acta Mater.* 58 (2011) 5440.
- [42] N.D.M. Hine, K. Frensch, W.M.C. Foulkes, M.W. Finnis, *Phys. Rev. B* 79 (2009) 024112.
- [43] J.L. Smialek, N.S. Jacobson, B. Gleeson, D.B. Hovis, A.H. Heuer, *NASA/TM* (2013) 217855.
- [44] D. Naumenko, B. Gleeson, E. Wessel, L. Singheiser, W.J. Quadakkers, *Met. Mater. Trans. A* 38A (2007) 2974.
- [45] K. Messaoudi, A.M. Huntze, B. Lesage, *Mater. Sci. Eng. A* A247 (1998) 248.
- [46] T.A. Ramanarayanan, M. Raghavan, R. Petkovic-Luton, *J. Electrochem. Soc.* 131 (1984) 923.
- [47] B.A. Pint, in: fourth ed. Shreir's Corrosion, vol. 1, 2010, pp. 606–645.
- [48] D.J. Young, D. Naumenko, L. Niewolak, E. Wessel, L. Singheiser, W.J. Quadakkers, *Mater. Corros.* 61 (2010) 838.
- [49] J. Ehlers, D.J. Young, E.J. Smaardyk, A.K. Tyagi, J. Penkalla, L. Singheiser, W.J. Quadakkers, *Corros. Sci.* 48 (2006) 3428.
- [50] G.C. Wood, I.G. Wright, T. Hodgkiess, D.P. Whittle, *Werkst. Korros.* 21 (1970) 900.
- [51] C.S. Giggins, F.S. Pettit, *Trans. AIME* 245 (1969) 2495.
- [52] J.E. Croll, G.R. Wallwork, *Oxid. Met.* 4 (1972) 121.
- [53] P. Kofstad, High Temperature Corrosion, Elsevier, London, 1988.
- [54] J.H. Park, W.E. King, S.J. Rothman, *J. Amer. Ceram. Soc.* 70 (1987) 880.
- [55] A.M. Huntz, S.C. Tsai, J. Balmain, K. Messaoudi, B. Lesage, C. Dolin, *Mater. Sci. Forum* 251–254 (1997) 313.
- [56] H.G. Sockel, B. Saal, M. Heilmaier, *Surf. Interface Anal.* 12 (1988) 531.
- [57] M.J. Graham, J.I. Eldridge, D.F. Mitchell, R.J. Hussey, *Mater. Sci. Forum* 43 (1989) 207.
- [58] R.E. Lobnig, H.P. Schmidt, K. Hennesen, H.J. Grabke, *Oxid. Met.* 37 (1992) 81.
- [59] L.B. Susanto, D.J. Young, *Mater. Corros.* 57 (2006) 474.
- [60] E.J. Felten, *Oxid. Met.* 10 (1976) 23.
- [61] C.W. Corti, D.R. Coupland, G.L. Selman, *Platinum Metals Rev.* 24 (1980) 2.
- [62] G.J. Tatlock, T.J. Hurd, *Oxid. Met.* 22 (1984) 201.
- [63] J.R. Nicholls, *MRS Bull.* 28 (2003) 659.
- [64] K. Bouhanek, O.A.A. Desanya, F.H. Stott, P. Skeldon, D.G. Lees, G.C. Wood, *Mater. Sci. Forum* 369–372 (2001) 615.
- [65] B. Gleeson, W. Wang, S. Hayashi, D. Sordelet, *Mater. Sci. Forum* 461–464 (2004) 213.
- [66] Y. Zhang, J.A. Haynes, B.A. Pint, I.G. Wright, *Surf. Coat. Technol.* 200 (2005) 1259.
- [67] S. Hayashi, S.I. Ford, D.J. Young, D.J. Sordelet, M.F. Besser, B. Gleeson, *Acta Mater.* 53 (2005) 3319.
- [68] E.H. Copland, *Acta Mater.* 55 (2007) 4853.
- [69] E.H. Copland, *J. Phase Equilibrium Diffusion* 28 (2007) 38.
- [70] Y. Ikeda, K. Nii, K. Yoshihara, *Trans. Jpn. Inst. Met.* 24 (1983) 207.
- [71] A.W. Funkenbush, J.G. Smeggill, N.S. Bornstein, *Met. Trans. A* 16A (1985) 1164.
- [72] J.G. Smeggill, A.W. Funkenbush, N.S. Bornstein, *Met. Trans. A* 17A (1985) 923.
- [73] D.G. Lees, *Oxid. Met.* 27 (1987) 75.
- [74] J.L. Smialek, *Met. Trans. A* 22A (1991) 739.
- [75] P.Y. Hou, *Oxid. Met.* 52 (1999) 337.

- [76] D. Oquab, D. Monceau, *Scripta Mat.* 44 (2001) 1147.
- [77] R. Rivoland, V. Maurice, P. Josso, M.-P. Bacos, P. Marcus, *Oxid. Met.* 60 (2003) 159.
- [78] J.A. Haynes, Y. Zhang, W.Y. Lee, B.A. Pint, I.G. Wright, K.M. Cooley, in: J.M. Hampikian, N.B. Dahotre (Eds.), *Elevated Temperature Coatings: Science and Technology III*, Minerals, Metals, Mater. Soc., Warrendale, PA, 1999, p. 185.
- [79] B.A. Pint, I.G. Wright, W.Y. Lee, Y. Zhang, K. Prüßner, K.B. Alexander, *Mater. Sci. Eng. A* 245 (1998) 201.
- [80] P.A. Van Manen, G.W.R. Leibbrandt, R. Klumpes, J.H.W. De Wit, *J. Phys. IV* 3 (1993) 123.
- [81] Y. Zhang, W.Y. Lee, J.A. Haynes, I.G. Wright, B.A. Pint, K.M. Cooley, P.K. Liaw, *Met. Mat. Trans. 30A* (1999) 1.
- [82] Y. Cadoret, M.-P. Bacos, P. Josso, V. Maurice, P. Marcus, S. Zanna, *Mater. Sci. Forum* 461–464 (2004) 247.
- [83] Y. Cadoret, D. Monceau, M.-P. Bacos, P. Josso, V. Maurice, P. Marcus, *Oxid. Met.* 64 (2005) 185.
- [84] S. Hayashi, T. Narita, B. Gleeson, *Mater. Sci. Forum* 522–523 (2006) 229.
- [85] G.C. Wood, F.H. Stott, in: R.A. Rapp (Ed.), *High Temperature Corrosion*, NACE, Houston, TX, 1983, p. 227.
- [86] F.H. Stott, G.C. Wood, J. Stringer, *Oxid. Met.* 44 (1995) 113.
- [87] S.M. Merchant, M.R. Notis, *Mater. Sci. Engg.* 66 (1984) 47.
- [88] E. Scheil, E.H. Schulz, *Arch. Eisenhüttenw.* 6 (1932) 155.
- [89] G.R. Wallwork, A.Z. Hed, *Oxid. Met.* 3 (1971) 171, 213, 229, 243.
- [90] G.R. Wallwork, *Rep. Prog. Phys.* 39 (1976) 401.
- [91] C.S. Giggins, F.S. Pettit, *J. Electrochem. Soc.* 118 (1971) 1782.
- [92] B.H. Kear, F.S. Pettit, D.E. Fornwalt, L.P. Lemaire, *Oxid. Met.* 3 (1971) 557.
- [93] C. Wagner, *Corros. Sci.* 5 (1965) 751.
- [94] J.S. Dunn, *J. Inst. Metals* 46 (1931) 25.
- [95] L.E. Price, G.J. Thomas, *J. Inst. Metals* 63 (1938) 21.
- [96] W.W. Smeltzer, D.P. Whittle, *J. Electrochem. Soc.* 125 (1978) 1116.
- [97] J.A. Nesbitt, R.W. Heckel, *Met. Trans. A* 18A (1987) 2075.
- [98] Y. Niu, F. Gesmundo, *Oxid. Met.* 56 (2001) 517.
- [99] W.E. Boggs, *Oxid. Met.* 10 (1976) 277.
- [100] H.C. Yi, S.W. Guan, W.W. Smeltzer, A. Petric, *Acta Metal. Mater.* 42 (1994) 981.
- [101] S.W. Guan, H.C. Yi, W.W. Smeltzer, *Oxid. Met.* 41 (1994) 377.
- [102] H.C. Yi, S.Q. Shi, W.W. Smeltzer, A. Petric, *Oxid. Met.* 43 (1995) 115.
- [103] H.C. Yi, W.W. Smeltzer, A. Petric, *Oxid. Met.* 45 (1996) 281.
- [104] F.H. Stott, *Mater. Sci. Tech.* 4 (1988) 431.
- [105] M. Schutze, *Oxid. Met.* 44 (1995) 29.
- [106] H.E. Evans, R.C. Lobb, *Corros. Sci.* 24 (1984) 209.
- [107] J.G. Smeggill, *Mater. Sci. Eng.* 87 (1987) 261.
- [108] J.L. Smialek, D.T. Jayne, J.C. Schaeffer, W.C. Murphy, *Thin Solid Films* 253 (1994) 285.
- [109] J.L. Smialek, R. Browning, in: Z.A. Munir, D. Cubicciotti (Eds.), *High Temp. Mater. Chem.*, Electrochemical Society Inc., Pennington, NJ, 1986, p. 258.
- [110] J.L. Smialek, *Met. Trans. A* 18A (1987) 164.
- [111] J.L. Smialek, B.K. Tubbs, *Met. Trans. A* 26A (1995) 427.
- [112] J.L. Smialek, B.A. Pint, *Mater. Sci. Forum* 369–372 (2001) 459.
- [113] C.L. Briant, K.L. Luthra, *Met. Trans. A* 19A (1988) 2099.
- [114] D. Fox, D.G. Lees, G.W. Lorimer, *Oxid. Met.* 36 (1991) 491.

- [115] P.Y. Hou, J. Stringer, *Oxid. Met.* 38 (1992) 323.
- [116] D.R. Sigler, *Oxid. Met.* 29 (1988) 23.
- [117] H.J. Schmutzler, H. Viefhaus, H.J. Grabke, *Surf. Interface Anal.* 18 (1992) 581.
- [118] V.K. Tolpygo, H.J. Grabke, *Oxid. Met.* 41 (1994) 343.
- [119] H.J. Grabke, G. Kurbatov, H.J. Schmutzler, *Oxid. Met.* 43 (1995) 97.
- [120] A.M. Huntz, G.B. Abderrazik, G. Moulin, E.W.A. Young, J.H.W. de Wit, *App. Surf. Sci.* 28 (1987) 345.
- [121] I.G. Wright, B.A. Pint, in: Proc. SF2M 2000: Journées d'automne, Société Francaise de Metallurgie et de Materiaux, Paris, 2000, p. 86.
- [122] V.K. Tolpygo, H.J. Grabke, *Scripta Mater.* 38 (1998) 123.
- [123] K.P.R. Ready, J.L. Smialek, A.R. Cooper, *Oxid. Met.* 17 (1989) 429.
- [124] W.J. Quadakkers, H. Holzbrecher, K.G. Brief, H. Beske, *Oxid. Met.* 32 (1989) 67.
- [125] E. Schumann, J.C. Yang, M.J. Graham, M. Ruhle, *Werkst. Korros.* 47 (1996) 631.
- [126] F.H. Stott, *Mater. Sci. Forum* 251–254 (1997) 19.
- [127] P.A. Van Manen, E.W.A. Young, D. Schalkoard, C.J. Van der Wekken, J.H.W. de Wit, *Surf. Interface Anal.* 12 (1988) 391.
- [128] P. Kofstad, K.P. Lillerud, *Oxid. Met.* 17 (127) (1982) 182.
- [129] H. Hindam, W.W. Smeltzer, *Oxid. Met.* 14 (1980) 337.
- [130] F.A. Golightly, F.H. Stott, G.C. Wood, *Oxid. Met.* 10 (1976) 163.
- [131] B.A. Pint, *Oxid. Met.* 45 (1996) 1.
- [132] F.N. Rhines, J.S. Wolf, *Met. Trans.* 1 (1970) 1701.
- [133] C.M. Cotell, G.J. Yurek, R.J. Hussey, D.F. Mitchell, M.J. Graham, *Oxid. Met.* 34 (1990) 173.
- [134] J. Zurek, D.J. Young, E. Essmann, M. Hansell, H.J. Penkalla, L. Niewolak, W.J. Quadakkers, *Corros. Sci.* 48 (2006) 3428.
- [135] A.G. Evans, G.B. Cromley, R.E. Demaray, *Oxid. Met.* 20 (1983) 193.
- [136] L.B. Pfeil, U.K. Patent No. 459848, 1937.
- [137] D.P. Whittle, J. Stringer, *Phil. Trans. Roy. Soc. Lond. A* 295 (1980) 309.
- [138] J. Stringer, *Mater. Sci. Eng. A* 120 (1989) 129.
- [139] R. Prescott, M.J. Graham, *Oxid. Met.* 38 (1992) 233.
- [140] S. Chevalier, *Mater. Corros.* 65 (2014) 109.
- [141] B.A. Pint, J.R. Martin, L.W. Hobbs, *Oxid. Met.* 39 (1983) 167.
- [142] R. Prescott, D.F. Mitchell, M.J. Graham, J. Doychak, *Corros. Sci.* 37 (1995) 1341.
- [143] R.A. Versaci, D. Clemens, W.J. Quadakkers, R. Hussey, *Solid State Ionics* 59 (1993) 235.
- [144] O.T. Goncel, J. Stringer, D.P. Whittle, *Corros. Sci.* 18 (1978) 701.
- [145] K. Przybylski, A.J. Garratt-Reed, G.J. Yurek, *J. Electrochem. Soc.* 135 (1988) 509.
- [146] K. Przybylski, G.J. Yurek, *J. Electrochem. Soc.* 135 (1988) 517.
- [147] B.A. Pint, A.J. Garratt-Reed, L.W. Hobbs, *Mater. High Temp.* 13 (1995) 3.
- [148] K.Y. Kim, S.H. Kim, K.W. Kwon, I.H. Kim, *Oxid. Met.* 41 (1994) 179.
- [149] P. Choquet, R. Mevrel, *Mater. Sci. Eng. A* 120 (1989) 153.
- [150] A. Glazkov, M. Gobel, G. Borchadt, H. Al-Badairy, G.J. Tatlock, J. Le Coze, in: S.B. Newcomb, J.A. Little (Eds.), *Microscopy of Oxidation-3*, Institute of Materials, London, 1997, p. 115.
- [151] P.Y. Hou, in: P.Y. Hou, M.J. McNallan, R. Oltra, E.J. Opila, D.A. Shores (Eds.), *High Temperature Corrosion and Materials Chemistry*, Electrochemical Society, Pennington, NJ, 1998, p. 198.
- [152] K. Prussner, E. Schumann, M. Ruhle, in: D.A. Shores, R.A. Rapp, P.Y. Hou (Eds.), *Fundamental Aspects of High Temperature Corrosion*, Electrochemical Society, Pennington, NJ, 1996, p. 344.

- [153] T.N. Rhys-Jones, H.J. Grabke, H. Kudielka, *Werkst. Korros* 38 (1987) 65.
- [154] P.Y. Hou, J. Stringer, *Oxid. Met.* 29 (1988) 45.
- [155] J. Stringer, B.A. Wilcox, R.I. Jaffee, *Oxid. Met.* 5 (1972) 11.
- [156] P.Y. Hou, *J. Am. Ceram. Soc.* 86 (2003) 660.
- [157] B. Gleeson, M.A. Harper, in: M. Schutze, W.J. Quadakkers, J.R. Nicholls (Eds.), *Lifetime Modelling of High Temperature Corrosion Processes*, Institute of Materials, London, 2001, p. 167.
- [158] B.A. Pint, J.A. Haynes, K.L. More, I.G. Wright, C. Leyens, in: K.A. Green, T.M. Pollock, R.D. Kissinger (Eds.), *Superalloys 2000*, TMS Warrendale, PA, 2000, p. 629.
- [159] M.J. Bennett, J.B. Price, *J. Mater. Sci.* 16 (1981) 170.
- [160] D.J. Young, *High Temp. Tech.* 1 (1982) 101.
- [161] H.E. Evans, D.A. Hilton, R.A. Holm, S.J. Webster, *Oxid. Met.* 19 (1983) 1.
- [162] A.G. Revsz, F.P. Fehlner, *Oxid. Met.* 15 (1981) 297.
- [163] M.J. Bennett, J.A. Desport, P.A. Labun, *Oxid. Met.* 22 (1984) 291.
- [164] D.L. Douglass, J.S. Armijo, *Oxid. Met.* 2 (1970) 207.
- [165] S. Sheybani, D.L. Douglass, *Oxid. Met.* 29 (1988) 307; 30 (1989) 433.
- [166] A. Kumar, D.L. Douglass, *Oxid. Met.* 10 (1976) 1.
- [167] R.N. Durham, B. Gleeson, D.J. Young, *Oxid. Met.* 50 (1998) 139.
- [168] B. Ahmad, P. Fox, *Oxid. Met.* 52 (1999) 113.
- [169] D.E. Jones, J. Stringer, *Oxid. Met.* 9 (1975) 409.
- [170] R.N. Durham, B. Gleeson, D.J. Young, *Mater. Corros.* 49 (1999) 855.
- [171] G.R. Johnston, *High Temp. High Press.* 14 (1982) 695.
- [172] B. Li, B. Gleeson, *Oxid. Met.* 65 (2006) 101.
- [173] I.-H. Jung, *Solid State Ionics* 177 (2006) 765.
- [174] A. Naoumidis, H.A. Schulze, W. Jungen, P. Lersch, *J. Eur. Ceram. Soc.* 7 (1991) 55.
- [175] O. Kubaschewski, C.B. Alcock, P.J. Spencer, *Materials Thermochemistry*, sixth ed., Pergamon, Oxford, 1993.
- [176] A.S. Nagelberg, *Oxid. Met.* 17 (1982) 415.
- [177] J.H. Chen, P.M. Rogers, J.A. Little, *Mater. Sci. Forum* 251–254 (1997) 57.
- [178] D.R. Sigler, *Oxid. Met.* 46 (1996) 335.
- [179] C. Leyens, B.A. Pint, I.G. Wright, *Surf. Coatings Tech.* 133–134 (2000) 15.
- [180] P.Y. Hou, X.F. Zhang, R.M. Cannon, *Scripta Mater.* 50 (2004) 45.
- [181] M.P. Harmer, cited in [156].
- [182] D. Oquab, D. Monceau, *Scripta Mater.* 44 (2001) 2741.
- [183] R. Kartono, D.J. Young, *Mater. Corros.* 59 (2008) 1.
- [184] C.T. Fujii, R.A. Meussner, *J. Electrochem. Soc.* 114 (1967) 435.
- [185] J.A. Colwell, R.A. Rapp, *Met. Trans. A* 17A (1986) 1065.
- [186] X.A. Zheng, D.J. Young, *Oxid. Met.* 42 (1994) 163.
- [187] H.E. McCoy, *Corrosion* 21 (1965) 84.
- [188] M. Hansel, C.A. Boddington, D.J. Young, *Corros. Sci.* 45 (2003) 967.
- [189] A. Schnaas, H.J. Grabke, *Oxid. Met.* 12 (1978) 387.
- [190] R.A. Holm, H.E. Evans, *Werkst. Korros* 38 (1987) 224.
- [191] X.G. Zheng, D.J. Young, *Corros. Sci.* 38 (1996) 1877.
- [192] X.G. Zheng, D.J. Young, *Mater. Sci. Forum* 251–254 (1997) 567.
- [193] R.E. Lobnig, H.J. Grabke, *Corros. Sci.* 30 (1990) 1045.
- [194] F.H. Stott, F.M.F. Chong, C.A. Stirling, in: *Proc. Int. Congress Metallic Corros.*, vol. 2, National Research Council of Canada, Ottawa, 1984, p. 1.
- [195] S. Sheybani, D.L. Douglass, *Oxid. Met.* 307; 30 (1989) 433.

- [196] D.R.G. Mitchell, D.J. Young, *J. Mater. Sci. Lett.* 12 (1993) 1076.
- [197] J.K.R. Weber, M.G. Hocking, *Oxid. Met.* 32 (1989) 1.
- [198] S. Taniguchi, T. Shibata, T. Niida, *Oxid. Met.* 34 (1990) 277.
- [199] S.-C. Kung, V. Srinivasan, *Oxid. Met.* 33 (1990) 481.
- [200] E.C. Potter, G.M.W. Mann, in: *Proc. 2nd Int. Congress Metallic Corros.*, NACE, New York, 1963, p. 872.
- [201] A. Atkinson, *Rev. Mod. Phys.* 57 (1985) 437.
- [202] L. Tomlinson, N.J. Cory, *Corros. Sci.* 29 (1989) 939.
- [203] M.R. Taylor, J.M. Calvert, D.G. Lees, D.B. Meadowcroft, *Oxid. Met.* 14 (1980) 497.
- [204] F. Rouillard, G. Moine, L. Martinelli, J.C. Ruiz, *Oxid. Met.* 77 (2012) 27.
- [205] L. Martinelli, F. Balbaud-Celerier, A. Terlain, S. Bosonnet, G. Picard, G. Santarini, *Corros. Sci.* 50 (2008) 2537.
- [206] M.G.C. Cox, B. McEnerney, V.D. Scott, *Phil. Mag.* 26 (1972) 839.
- [207] G.B. Gibbs, *Oxid. Met.* 7 (1973) 73.
- [208] G.B. Gibbs, R. Hales, *Corros. Sci.* 17 (1977) 487.
- [209] J. Robertson, M.I. Manning, *Mater. Sci. Tech.* 4 (1988) 1064.
- [210] L.B. Pfeil, *J. Iron Steel Inst.* 119 (1929) 501.
- [211] A. Dravnieks, H.J. McDonald, *J. Electrochem. Soc.* 94 (1948) 139.
- [212] A. Bruckman, J. Romanski, *Corros. Sci.* 5 (1965) 185.
- [213] S. Mrowec, T. Werber, *Corros. Sci.* 5 (1965) 717.
- [214] S. Mrowec, *Corros. Sci.* 7 (1967) 563.
- [215] D.J. Young, H. Yin, *Oxid. Met.* 79 (2013) 445.
- [216] W.W. Smeltzer, *Acta Mat.* 8 (1960) 377.
- [217] H.E. Evans, *Mat. Sci. Technol.* 4 (1988) 1089.
- [218] D.J. Young, J. Zurek, L. Singheiser, W.J. Quadakkers, *Corros. Sci.* 53 (2011) 2131.